Alma Mater Studiorum · Università di Bologna

Dipartimento di Fisica e Astronomia "Augusto Righi"

Laurea Magistrale in Fisica del Sistema Terra

Inversion of IASI observations in all-sky conditions

Relatore:

Prof. Tiziano Maestri

Correlatore:

Dott. Michele Martinazzo

Presentata da:

Alicia Prestini

Anno Accademico 2024/2025

Abstract

This thesis investigates the performance of the inversion code IOTA, based on the radiative transfer model σ, under all-sky conditions using observations from the Infrared Atmospheric Sounding Interferometer (IASI). Retrievals in the presence of scattering particles like aerosols are particularly important, as operational algorithms still show limited capability under these conditions, especially in the infrared.

IOTA relies on the Optimal Estimation approach and employs PCA state compression. Aerosol prior information is introduced through an ad-hoc covariance matrix that produces physically plausible vertical profiles while providing regularization for the inversion.

First, the robustness of the inversion framework is assessed under clear-sky conditions. Then, a subset of aerosol-affected cases is analyzed by performing the inversion including dust parameters in the state vector. The results are evaluated through two approaches: temperature and humidity profiles are validated against radiosonde measurements and the internal consistency of the retrieval is assessed through statistical diagnostics. The retrieval results show good agreement with radiosonde measurements and a clear gain of information during the retrieval is observed. The aerosol retrieval experiments indicate a measurable sensitivity of both the instrument and the inversion algorithm to dust, allowing the retrieval of aerosol content and effective radius profiles. When aerosols are included in the retrieval for cases where they are detected, an improvement is observed both in the agreement with radiosonde measurements and in the statistical analysis compared to the clear-sky configuration. The results demonstrate that the IOTA inversion framework can handle atmospheric conditions including aerosols, and that its performance improves when a more realistic and complex description of the atmospheric state is incorporated into the retrieval process.

Contents

Chapter 1

Introduction

1.1 Satellite observations and retrieval of temperature and humidity

Over the past decades, satellite remote sensing has profoundly transformed our ability to observe and understand the Earth system. From weather forecasting to climate monitoring and atmospheric composition studies, spaceborne instruments provide global, continuous, and homogeneous measurements that are unattainable with ground-based networks alone. In particular, hyperspectral infrared sounders like the Infrared Atmospheric Sounding Interferometer (IASI) [1] have revolutionized atmospheric profiling by sampling the thermal emission spectrum in thousands of narrow channels across key absorption bands of CO_2, H_2O, O_3, and other gases, thereby enabling the retrieval of temperature, humidity, and trace-gas distributions with unprecedented vertical resolution and accuracy. By resolving the vertical structure of the atmosphere, these instruments directly constrain the radiative energy budget, moist processes, and large-scale dynamics that underpin both weather and climate variability. Satellite instruments, however, do not directly measure the atmospheric variables of interest; instead, they observe radiances at the top of the atmosphere that are related to the atmospheric state through the radiative transfer equation. The mapping from state to radiance is nonlinear, vertically integrated through weighting functions, and affected by instrumental noise and forward-model imperfections. Retrieving geophysical profiles therefore requires solving an inverse problem, in which one seeks the most probable atmospheric state consistent with the observations, the measurement and model errors, and prior constraints. This inverse problem is fundamentally ill-posed: small perturbations in the measurements can correspond to large changes in the inferred state, and multiple atmospheric profiles can fit the same radiance spectrum within its noise [2, 3].

As a result, modern physical retrieval schemes rely on Bayesian or optimal esti-

mation frameworks, which regularize the inversion by combining radiances with prior information and provide rigorous diagnostics of averaging kernels, error covariances, and information content. From an operational point of view, these retrievals are embedded in a broader data assimilation and forecasting chain. Most numerical weather prediction (NWP) centers currently assimilate hyperspectral infrared information predominantly in clear-sky or cloud-cleared form. This is because radiative transfer modeling in scattering conditions increases the non-linearity level of the problem. In addition, cloud layers usually constitute a sharp discontinuity with respect to the clear sky case, thus increasing the ill-posed nature of the problem. In practice, this means that only channels and footprints that are judged to be unaffected (or only weakly affected) by clouds and aerosols are used directly. For similar reasons, IASI does not provide retrieval products (e.g., thermodynamical profiles) when clouds are detected in the scene. On the other hand, when a scene is classified as clear-sky, operational IASI products typically include vertical profiles of temperature, humidity, ozone, together with surface properties (emissivity and temperature) and trace gases (e.g., total column of CO_2, N_2O and CH_4). IASI temperature and humidity retrievals rely on sophisticated inversion schemes implemented in NWP centers [4, 5] and under clear-sky conditions exhibit typical uncertainties of about $\simeq$ 1 K and $\simeq$ 1-1.5 g kg^{-1} in the troposphere, as demonstrated by dedicated validation studies [6, 7]. Temperature and water vapor are the key thermodynamic variables controlling atmospheric dynamics and the radiative energy balance. For this reason, it is essential to retrieve their vertical distributions with the highest possible accuracy. In this context, the validation of satellite-derived products through comparison with independent in situ measurements, such as radiosonde observations, is crucial to assess their reliability. In particular, validation studies of IASI temperature and humidity retrievals have shown a very good overall agreement with radiosonde measurements [8, 9].

Despite the maturity of these operational products, they are generally designed for and applied under clear-sky conditions. In realistic atmospheric scenes, the presence of clouds and aerosols introduces scattering and absorption processes that considerably complicate the radiative transfer and inversion problem. This highlights the need to investigate, develop and validate retrieval approaches capable of operating under all-sky conditions, such as the scheme proposed in this work.

It is important to note that, in recent years, another class of inversion methods has been developed: namely, data-driven approaches. These methods exploit machine learning techniques to extract non-linear relationships between the observations and the atmospheric state. They can be extremely efficient from a computational standpoint. However, they rely on the availability of a representative dataset used for training and

the interpretation of the results is not straightforward due to the lack of explicit physics and diagnostic objects such as averaging kernels.

1.2 Retrieval of aerosol in the infrared

While clear-sky conditions provide a controlled environment for algorithm assessment, the real atmosphere is rarely aerosol-free. Mineral dust, volcanic ash, and anthropogenic pollution modify radiance signals through absorption and scattering processes. Spectral signatures associated with specific particle types can alter atmospheric window regions and introduce biases in temperature and humidity retrievals if not explicitly modeled.

Beyond their impact on remote sensing observables, aerosols are a key component of the Earth system because they affect climate through both direct interactions with radiation and indirect effects mediated by clouds and precipitation. These processes remain among the main contributors to uncertainty in estimates of aerosol effective radiative forcing, particularly for aerosol–cloud interactions [10]. In addition, aerosols pose a major risk to human health, contributing to respiratory and cardiovascular diseases and substantial premature mortality worldwide. Improving aerosol detection and characterization is therefore important not only for algorithmic robustness, but also for climate studies and air-quality applications.

Most satellite-based aerosol retrieval techniques have traditionally been developed in the visible and ultraviolet spectral regions, where scattering processes dominate and aerosol optical depth can be retrieved with high sensitivity. Several operational algorithms have been developed for this purpose, for example the MODIS Aerosol Algorithm which exploits spectral reflectance measurements to derive aerosol optical properties over different surface types [11]. Multi-angle observations, such as those from the MISR instrument, further improve aerosol retrievals by using directional reflectance information to better separate surface and atmospheric contributions [12]. These approaches have enabled the generation of long-term global aerosol datasets. However, retrievals based on solar radiation are intrinsically limited to daytime observations and are strongly affected by uncertainties in surface reflectance, particularly over bright surfaces such as deserts, snow-covered regions, and urban areas. These limitations motivate the exploration of complementary retrieval approaches based on thermal infrared measurements.

Thermal infrared observations provide several advantages for aerosol detection. Because they rely on emitted radiation rather than reflected sunlight, they allow observations during both day and night and are less sensitive to surface reflectance effects. In

the thermal infrared, aerosol effects are generally weaker than in the solar spectrum, but they remain detectable, and infrared sounders such as IASI have demonstrated sensitivity to aerosol absorption features, particularly for coarse-mode particles such as mineral dust. Several studies have shown that thermal infrared radiances can be used to retrieve aerosol properties including aerosol optical depth and layer altitude [13]. In addition, developments in radiative transfer modeling have enabled the extension of retrieval frameworks from clear-sky to more complex atmospheric conditions. Physically based scaling methods allow cloud and aerosol optical properties to be incorporated into fast radiative transfer models [14, 15, 16]. By enabling the treatment of multiple scattering effects without compromising computational efficiency [17], these approaches pave the way toward full-spectrum, physically consistent all-sky inversion schemes.

Dedicated algorithms and products, such as the IASI Dust Flag [18] and vertical aerosol profiling schemes, have been evaluated against ground-based observations, showing significant correlation in the identification dust loading and structure. For example, the MAPIR algorithm retrieves vertical dust concentration profiles from IASI observations using an optimal estimation framework applied to selected atmospheric window spectral regions [19, 20]. However, this algorithm relies on rather specific and strongly constrained assumptions on the initial guess of the thermodynamic profiles. More generally, many existing all-sky retrieval approaches simplify the representation of atmospheric scatterers (aerosols or clouds) by reducing them to one or two homogeneous layers or by retrieving only bulk properties such as optical depth [21]. While these studies demonstrate the potential of infrared measurements for aerosol characterization and highlight the complementary information that infrared observations can provide relative to visible and ultraviolet retrievals, aerosol retrieval in the thermal infrared remains less mature than in the solar spectrum. This underlines the need to develop and test retrieval schemes capable of exploiting infrared information without relying on overly restrictive assumptions. In this context, the scheme proposed in this work enables the retrieval of the full vertical profiles of aerosol particle radius and mass mixing ratio by introducing an ad-hoc covariance matrix to regularize the inversion, while avoiding additional structural constraints.

1.3 Objectives and overview

In this framework, the primary objective of this study is to assess the physical consistency and robustness of the newly implemented inversion algorithm IOTA, coupled with the forward model SIGMA [22] applied to IASI radiances [23, 8] collocated with

radiosonde observations used for validation.

The analysis is first carried out by focusing on retrievals performed under clear-sky conditions, in order to evaluate the algorithm in a relatively simple and controlled framework. In a second step, the retrievals are extended to include aerosol effects, using a subset of observations characterized by the presence of dust, in order to investigate the capability of the model to operate under more complex scattering conditions.

The evaluation is performed by validating the retrieved temperature and humidity profiles against independent radiosonde measurements collected at the San Pietro Capofiume (Bologna, Italy) station [24], providing an independent and highly accurate reference. In addition, an internal assessment of the retrieval performance is conducted by analyzing the spectral residuals between observed and simulated radiances and by examining the distributions of the χ^2 statistic.

While the present analysis focuses mainly on mineral dust aerosols, the radiative transfer framework adopted in this study is formulated in a general way. Owing to the physical parameterizations implemented in the forward model, the methodology can in principle be extended to investigate the radiative effects of different types of atmospheric scatterers, allowing the framework to be applied to a broader range of aerosol and cloud conditions.

The remainder of this thesis is organized as follows. In Chapter 2, the fundamental theoretical background of the forward model and the inversion model is presented, outlining the main physical assumptions and mathematical framework. Chapter 3 describes the datasets and the methodology adopted for the analysis. Finally, Chapter 4 presents and discusses the results, highlighting the main findings and their implications.

Chapter 2

Theoretical background

In this part, we further develop the theoretical framework and outline the essential concepts required to understand the IOTA inversion model and the results discussed later. We first describe the structure and physical assumptions of the forward model SIGMA, followed by a discussion of the main features of the inversion scheme. The section concludes with a brief introduction to atmospheric aerosols and their key physical and optical properties.

2.1 Forward model SIGMA

2.1.1 Radiative transfer

The radiative transfer model σ used in this study is based on a one-dimensional geometry, pseudo-monochromatic fast code that computes the infrared spectrum [22, 15, 16, 25]. The forward model takes as input all the relevant physical parameters, contained within a state vector, and simulates the corresponding radiation field. It is closely linked to the actual observations being performed and reflects the underlying physics of the measurements. Additionally, it incorporates information about the instrument characteristics and the associated measurement noise. The problem can be generally described by the equation:

$$\mathbf{I} = F(\mathbf{x}) + \boldsymbol{\varepsilon} \tag{2.1}$$

where $\boldsymbol{I}$ is the measured radiance, F is the model as a function of the state vector $\boldsymbol{x}$, mapping from the atmospheric state space to the observation space, and $\boldsymbol{\epsilon}$ is the error. F embodies all the physics that will be described in this section while $\boldsymbol{\epsilon}$ describes the instrumental error and the error in the model. F basically solves the equation of radiative transfer by calculating the total spectral radiance I_ν in an additive model,

which can be written in this way:

$$I_\nu(\mu) = I^s_\nu(\mu) + I^a_\nu(\mu) + I^r_\nu(\mu) + I^i_\nu(\mu) \tag{2.2}$$

Where $I_\nu(\mu)$ is decomposed into four terms: the surface radiance at the top of the atmosphere $I^s_\nu(\mu)$, the atmospheric term $I^a_\nu(\mu)$, the contribution of the downward infrared radiation reflected at the surface $I^r_\nu(\mu)$ and the solar radiation reflected at the surface $I^i_\nu(\mu)$. All these components have a dependence on the wavenumber ν and over the directional angle $\mu = cos\theta$ where θ is the satellite zenith angle.

In Eq.2.2 the surface term can be written as:

$$I^s_\nu(\mu) = \epsilon_\nu \, B_\nu(T_s) \, Tr^0_\nu(\mu) \tag{2.3}$$

where ϵ_ν is the emissivity spectrum of the surface and B is the black-body Planck function, depending on the wavenumber and on the surface temperature T_s. $Tr^0_\nu(\mu)$ is the total spectral transmittance of the atmosphere, defined as:

$$Tr^0_\nu(\mu) = e^{-\frac{\tau^0_\nu}{\mu}}$$

where τ^0_ν is the total spectral optical depth of the atmosphere, combining both scattering and absorption effects. The optical depth of a layer z can be written as:

$$\tau_\nu(z) = \int_z^{z_{top}} dz \, \beta_\nu(z)$$

Where β_ν is the absorption coefficient, depending on the cross section and on the gases density.

Eq.2.3 is the radiance emitted from the surface and then transmitted by the atmosphere.

The atmospheric term is expressed as:

$$I^a_\nu(\mu) = \int_0^{z_{top}} dz \frac{\partial Tr_\nu(z,\mu)}{\partial z} B_\nu(T(z)) \tag{2.4}$$

Where $Tr_\nu(z,\mu)$ is the atmospheric transmittance from the emitting layer at level z to the top of the atmosphere (z_{top}). Eq.2.4 is the radiance emitted from each layer at a certain level z and then transmitted by the atmosphere from the level up to the top of the atmosphere, all integrated over the entire atmosphere.

The expression of term $I^r_\nu(\mu)$ depends on the type of surface, in particular it is defined for the sea surface using a specular model:

$$I^r_{\nu,sea}(\mu) = (1-\epsilon_\nu) \, Tr^0_\nu(\mu) \int_{z_{top}}^0 dz \frac{\partial Tr^d_\nu(z)}{\partial z} B_\nu(T(z))$$

where $Tr^d(z)$ is the down-welling transmittance from the level z to the surface $z = 0$. This term is the emitted radiance from a layer of the atmosphere, transmitted by the

atmosphere underneath, reflected by the surface and then transmitted by the entire atmosphere.

The surface term for land, the case of this work, is expressed using a Lambertian model:

$$I^r_{\nu,land}(\mu) = (1-\epsilon_\nu) Tr^0_\nu(\mu) \int_{z_{top}}^{0} dz \frac{\partial Tr^{d*}_\nu(z)}{\partial z} B_\nu(T(z)) \tag{2.5}$$

where $Tr^{d*}(z)$, the diffuse or slab down-welling transmittance, defined as:

$$Tr^{d*}_\nu(z) = 2\int_0^1 d\mu\, \mu\, Tr^d_\nu(z,\mu)$$

which is the down-welling transmittance when the radiance is coming from all the directions. In order to simplify this integral over all the angles, it can be calculated as the transmittance at a suitable cosine angle $\bar{\mu}$ so that:

$$Tr^*_\nu(z) \simeq Tr_\nu(\bar{\mu}, z) = e^{-\frac{\tau_\nu(z)}{\bar{\mu}}}$$

where $\frac{1}{\bar{\mu}}$ is referred to as the *diffusivity factor*. Based on numerical computations it can be shown that 1.66 a good approximation for this factor [26].

Eq.2.5 is the radiance emitted from each layer of the atmosphere, transmitted from that layer to the surface, reflected at the surface and transmitted by the atmosphere.

The solar radiance reflected at the surface is:

$$I^i_\nu(\mu) = (1-\epsilon_\nu) Tr^0_\nu(\mu) \frac{F_\odot \mu_0}{\pi} Tr^0_\nu(\mu_0) \tag{2.6}$$

Where $Tr^0_\nu(\mu_0) = e^{-\frac{\tau^0_\nu}{\mu_0}}$ is the total atmospheric transmittance considering the solar zenith angle μ_0 and $F_\odot$ is the solar monochromatic irradiance. Eq.2.6 is the incoming solar radiation transmitted by the atmosphere, reflected from the surface and then transmitted again by the atmosphere. Considering the range of wavenumber in which σ works (100 - 2760 cm^{-1}) and the one that will be used in this work, this term is negligible, as its contribution becomes important above 2300 cm^{-1}, so that we will only focus on the first three terms of Eq.2.2.

2.1.2 SIGMA approximations and parametrization

Integral terms in Eq.2.4 and Eq.2.5 must be computed numerically in the model, to do that σ uses a finite atmospheric layering to compute optical depths. The layering consists of a fixed 60-layer pressure grid spanning the 1013-0.005 hPa range. The 61 pressure levels that divide the atmosphere into 60 (L) layers have a higher density above the tropopause, the optimal configuration to simulate this type of data (Fig.2.1) [22, 25]. Each layer has a homogeneous temperature and composition.

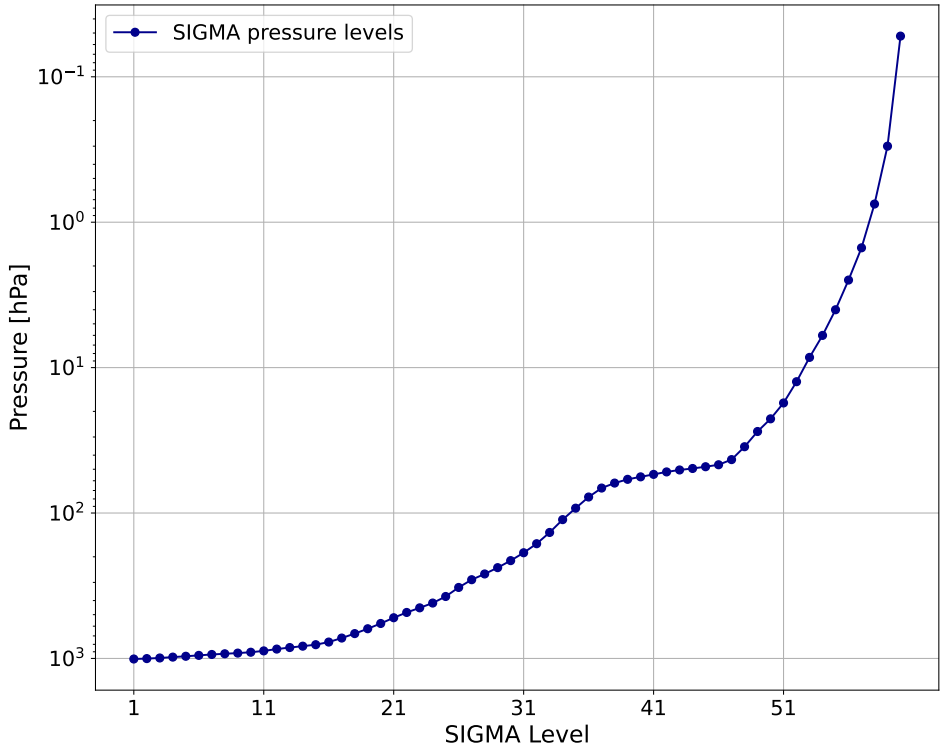

Figure 2.1: *Pressure of atmospheric levels defined in σ for a mid-latitude atmosphere*

In this way, the complete equation Eq.2.2 (dropping the angular and wavenumber dependencies for clearness):

$$I = \epsilon\, B(T_s)\, Tr^0 + \int_0^{z_{top}} dz \frac{\partial Tr}{\partial z} B(T) + (1-\epsilon) Tr^0 \int_{z_{top}}^{0} dz B(T) \frac{\partial Tr^{d*}}{\partial z}$$
$$+(1-\epsilon) Tr^0 \frac{F_\odot \mu_0}{\pi} Tr^0(\mu_0)$$

can be rewritten as [25]:

$$I \simeq \epsilon\, B(T_s)\, Tr^0 + \sum_{j=1}^{L} B(T_j)(Tr_j - Tr_{j-i})$$
$$+ (\epsilon - 1) Tr^0 \sum_{j=1}^{L} B(T_j)(Tr_j^d - Tr_{j-1}^d) + (1-\epsilon) Tr^0 \frac{F_\odot \mu_0}{\pi} Tr^0(\mu_0)$$

Chou approximation: clouds and aerosol

Eq.2.2 provides a general formulation that can represent both clear-sky and cloudy or aerosol-affected conditions. To highlight this property we define the parameter cf as the cloud fraction in a field of view of the satellite, so that $cf = 0$ corresponds to a clear field of view while $cf = 1$ to fully overcast one. In this way, the all-sky radiance is

computed as the linear combination of clear and cloudy terms, where each contribution is weighted by the cloud fraction:

$$I_\nu = (1 - cf) I_{\nu,clear-sky} + cf I_{\nu,cloudy-sky} \tag{2.7}$$

In the first part of the study we focus on clear-sky retrievals ($cf = 0$), while when aerosol retrievals are performed cf is set to 1. For a clear sky scenario, the model solves the equation considering a non-scattering atmosphere and only the absorption by atmospheric gases is considered. If clouds or aerosols are present, the equation becomes significantly more complex, as an adequate source function dealing with multiple scattering must be considered. The multiple scattering source function can be expressed as:

$$J_{multiple\ scattering}(\tau, \mu) = \frac{\omega_0}{2} \int_{-1}^{1} d\mu'\, \mu'\, I(\tau, \mu') P(\mu, \mu') \tag{2.8}$$

Where ω_0 is the single scattering albedo, defined as: $\frac{\tau_s}{\tau}$, the ratio between the optical depth related only to scattering processes and the total optical depth. $P(\mu, \mu')$ is the phase function that depends on the angle of the incoming radiation (μ') describing the probability of scattering into specific scattering angle (μ: the viewing angle of the satellite). P is defined for every geometry and dimension of the scattering particle. It is crucial to simplify this term in order to save computational time. For this reason the Chou approximation is used [17], allowing not to compute directly the term of multiple scattering. In this approximation the scattering contribution is accounted for by replacing the total extinction optical depth τ of a single layer with an apparent absorption optical depth $\tilde{\tau}$, in this way:

$$\tilde{\tau} = (1 - \omega_0)\tau + b\omega_0\tau \tag{2.9}$$

Where $1 - \omega_0$ represents the part of optical depth related to absorption processes (and emission, in the case of local thermodynamic equilibrium). b is the backscattering coefficient quantifying the hemispheric backscattered radiation, computed through the integration of the phase function as in Eq.2.8, defined as:

$$b = \frac{1}{2} \int_0^1 d\mu \int_{-1}^0 d\mu' P(\mu, \mu')$$

Chou provides a simplified expression of b as a polynomial fitting so that the integral all over the angles doesn't have to be computed. The fitting is:

$$b = 1 - \sum_{i=1}^{4} a_i g^{i-1}$$

where a_i are coefficients expansion term defined for the scattering particles and g is the asymmetry parameter defined as :

$$g = \frac{1}{2}\int_{-1}^{1} d\mu\, \mu\, P(\mu)$$

Given the material, phase, shape, size and wavenumber g is a fixed and tabulated parameter. When computing the upwelling radiance, this parametrization introduces acceptable errors in the mid-infrared, but is less accurate in the far-infrared, especially for clouds with optical depth bigger than 1. For this reason, Tang introduced another adjustment to the Chou scheme; however, it will not be applied in this work [14].

So, the first term of the right-side of Eq.2.9 represents the true absorption and the second term represent the multiple scattering approximation and with this new definition of the optical depth the radiative transfer equation can be rewritten as a Schwarzschild-like equation [16]. This approximation makes the radiative transfer equation formally identical to the clear-sky case, providing a more robust theoretical framework and offering significant advantages in terms of computational efficiency.

So, with the Chou approximation, optical depth of clouds and aerosol is computed. Liquid water clouds are represented by a particle size distribution (PSD) of spherical droplets; PSD is described by a lognormal distribution as a function of the effective radius r_{eff}. The single-scattering single particle radiative properties are calculated using a Mie solution based algorithm, implemented through the Scattnlay code [27], which provides scattering coefficients, phase function and efficiency factors. The refractive index of water is taken from [28]. These single-particle properties are subsequently integrated over the PSD to obtain the bulk single-scattering radiative properties.

Ice clouds are modeled as PSDs of non-spherical ice crystals. In natural ice cloud layers, a variety of crystal habits can occur depending on formation processes, cloud evolution, and thermodynamic conditions. In σ, ice particles are represented as aggregates composed of eight hexagonal ice columns, whose single-particle radiative properties are described in [29]. PSD for ice clouds is parameterized using a three-parameter gamma distribution as a function of the effective dimension D_{eff}.

Atmospheric aerosols exhibit a wide range of radiative characteristics due to variations in chemical composition, PSDs (often multimodal), and vertical concentration profiles. Although their dominant radiative impact occurs at short wavelengths (0.3–4 μm), certain aerosol types also produce non-negligible effects in the longwave spectral region (4–100 μm), which must therefore be included in radiative transfer calculations. For this study, dust-like aerosol is considered [16].

Transmittance computation

Given τ the optical depth of an atmospheric layer and $e^{-\tau}$ the transmittance at that level, the general expression for the transmittance at a level j is defined as:

$$Tr_j = \prod_{i=j+1}^{L} e^{-(\tau_{gas,i}+\tau_{aerosol,i}+\tau_{cloud,i})}$$

So that the contribution of atmospheric gases, aerosols and cloud is fully considered.

The atmospheric gases optical depth is computed based on the temperature and gas concentration of the j-th layer:

$$\tau_{gas,i} = q_{i,j}(c_{0,i,j} + c_{1,i,j}\Delta T + c_{2,i,j}\Delta T^2)$$

where $q_{i,j}$ is the concentration of the i-th gas and $\Delta T = T_{ref,j} - T_j$, with $T_{ref,j}$ comes from the reference temperature profile at which the coefficients c are computed and tabulated; T_j is the actual equivalent temperature of the j-th layer. This parametrization is used for all gases with exception for water vapor, parametrized as:

$$\tau^{gas}_{H_2O,j} = q_{H_2O,j}(c_{0,H_2O,j} + c_{1,H_2O,j}\Delta T + c_{2,H_2O,j}\Delta T^2 + c_{3,H_2O,j}q_{H_2O,j}) \tag{2.10}$$

The coefficients $c_{n,i,j}$ are stored in a LookUp Table computed with the *Line-By-Line Radiative Transfer Model by Atmospheric and Environmental Research* (LBLRTM) [30].

Considering the general form of the radiative transfer equation we can construct the state vector needed for the model and to fully calculate the radiance entering the satellite. The state vector ingested by the code is therefore the following:

$$\begin{aligned} x_{\sigma-IASI} = (&\epsilon,\, T,\, T_s,\, Q,\, O_3,\, HDO,\, q_{LWC},\, q_{IWC},\, r_{eff},\, D_{eff},\, q_{CO_2},\, q_{N_2O},\, q_{CO},\, q_{CH_4},\\ &q_{SO_2},\, q_{HNO_3},\, q_{NH_3},\, q_{OCS},\, q_{CF_4},\, cf,\, \mu,\, p_s) \end{aligned} \tag{2.11}$$

the state vector is composed of: spectral emissivity, temperature profile, surface temperature, mixing ratio profiles of water vapor, ozone, HDO, the mixing ratio of liquid and ice water and relative effective radii, the mixing ratio profiles of different gases, cloud fraction, the viewing zenith angle and the surface pressure. In our study, we will directly provide the following variables: ϵ, T, T_s, Q, O_3, HDO, cf, μ, p_s while the other parameters are taken from the climatology.

In this way, all the parameters to solve the radiative transfer equation are given and it can be solved by the forward model.

In the first part, as only clear sky scenarios are considered, all the variables related to the cloud will not be considered as the cloud fraction is set to zero.

2.2 Retrieval algorithm *IOTA*

In this section, the basis of the inversion algorithm *IOTA*, a physical method based on the optimal estimation (OE), is described. The structure is taken from [31].

The aim of the inversion is to find the optimal state vector $\hat{\boldsymbol{x}}$ given a measurement $\boldsymbol{y} = \boldsymbol{I}$ and prior information by inverting Eq.2.1, using an iterative process. In addition to $\hat{\boldsymbol{x}}$, the inverse model provides the associate error and Jacobian matrices.

An ill-posed problem

OE exploits the idea that the measurement, its error and the state vector can be represented as Gaussian distributions. So the aim of the retrieval will be to relate the probability density function *pdf* of the measurement to the *pdf* of the state. The forward model F maps the state into the measurement space. Since the measurement has an associated error $\hat{\boldsymbol{\epsilon}}$ even if F is a deterministic mapping, a point in the state space is mapped into a region in measurement space, determined by $\boldsymbol{S}_\epsilon$, the *pdf* of $\hat{\boldsymbol{\epsilon}}$. On the other hand, given a measurement $\boldsymbol{y}$, it could be the result of a mapping from anywhere in a region of state space described by some *pdf*, rather than from a single point. This non direct correspondence between the state and the measurement and the consequent non-uniqueness of the solution is part of the ill-posedness of the inversion problem. From a linearized perspective, this non-uniqueness can be formally understood through the concept of the null space of the Jacobian matrix: $\frac{\partial \boldsymbol{y}}{\partial \boldsymbol{x}} = \boldsymbol{K}$. When the forward model is linearized around a reference state, the relationship between perturbations in the state vector and perturbations in the measurements can be written as:

$$\delta \boldsymbol{y} = \boldsymbol{K} \delta \boldsymbol{x}$$

The null space of $\boldsymbol{K}$ consists of all perturbations $\delta \boldsymbol{x}_n$ such that:

$$\boldsymbol{K} \delta \boldsymbol{x}_n = 0$$

These directions in state space produce no change in the measurement space and are therefore fundamentally unobservable. The existence of a non-trivial null space implies that different atmospheric states can produce identical radiance spectra, making the inverse problem intrinsically non-unique. In practical satellite retrievals, the null space is often large because the number of independent pieces of information contained in the radiance spectrum is much smaller than the dimension of the state vector. As a consequence, certain combinations of parameters (for example, specific vertical structures) cannot be independently retrieved from the measurements alone and require additional constraints.

In addition to non-uniqueness, the inversion of satellite radiance spectra is affected by non-existence of the solution due to approximations in the forward model (since physical description of some phenomena is too complex) and the instrumental noise and instability due to discretization of parameters and the finite number of observations. Therefore, when dealing with ill-posed problems of this kind, the implementation of suitable regularization and stabilization strategies becomes essential. These include both physical approaches, such as the introduction of prior knowledge about the expected solution, and mathematical approaches, such as the adoption of specific statistical assumptions.

In this framework, a Bayesian approach is a very helpful way of looking at the noisy inverse problem, in which we have some prior understanding and want to update the understanding in the light of new information.

Prior information about the state, for example a climatology (i.e., the prior dataset with mean $\boldsymbol{x}_a$ and covariance matrix $\boldsymbol{S}_a = \mathbb{E}[(\boldsymbol{x} - \boldsymbol{x}_a)(\boldsymbol{x} - \boldsymbol{x}_a)^T]$), can also be conveniently described by a *pdf*, and is used to constrain the solution. Such prior knowledge can be thought of as a virtual measurement, as, like a real measurement, it provides us with an estimate of some function of the state, together with a measure of the accuracy of the estimate, albeit usually rather a poor one. Within the Optimal Estimation framework, the introduction of the a priori covariance matrix acts as a constraint that regularizes the null-space directions, ensuring a stable and physically consistent solution. In this sense, the prior supplies information for those components of the atmospheric state that are weakly constrained or unconstrained by the observations. In practice, however, reliable prior information is often difficult to obtain. It must frequently be assembled from heterogeneous sources of varying quality, such as climatological datasets or previous experiments. For this reason, the construction and proper use of the *a priori* state and its covariance matrix require careful consideration. The accuracy of the solution will depend strongly on the prior information used in the construction of the retrieval relative to the particular case being retrieved. If the current case is well represented by the prior dataset, then the retrieval will likely be reasonably accurate, but if the current case is poorly represented in the prior dataset (i.e., $\boldsymbol{x}$ is "far" from $\boldsymbol{x}_a$), then the accuracy of the retrieval will likely be poorer, especially if the forward model is nonlinear.

Furthermore, an inappropriate specification of the prior covariance can also affect the retrieval. If the covariance matrix imposes constraints that are too restrictive, the solution may be biased toward the prior state in the affected components. On the other hand, if the constraints are too weak and the measurements provide limited information, the retrieval uncertainty may become excessively large. For these reasons,

the selection of an appropriate prior dataset and covariance structure is a crucial step in the design of a robust retrieval algorithm. [2].

Bayesian approach and error analysis

Bayes' theorem tells us how to combine the knowledge about the forward model and the prior in terms of *pdf*. The theorem states that, given the prior *pdf* $P(\boldsymbol{x})$, the *pdf* of the measurement $\boldsymbol{y}$, $P(\boldsymbol{y})$, and the conditional *pdf* of $\boldsymbol{y}$ given $\boldsymbol{x}$ $P(\boldsymbol{y}|\boldsymbol{x})$, the conditional *pdf* of $\boldsymbol{x}$ given $\boldsymbol{y}$ $P(\boldsymbol{x}|\boldsymbol{y})$, the posterior *pdf* of the state when the measurement is given, is:

$$P(\boldsymbol{x}|\boldsymbol{y}) = \frac{P(\boldsymbol{y}|\boldsymbol{x})P(\boldsymbol{x})}{P(\boldsymbol{y})} \tag{2.12}$$

Assuming Gaussian distribution we can express $P(\boldsymbol{y}|\boldsymbol{x})$ and $P(\boldsymbol{x})$ as :

$$-2logP(\boldsymbol{y}|\boldsymbol{x}) = (\boldsymbol{y} - F(\boldsymbol{x}))^T \boldsymbol{S}_\epsilon^{-1}(\boldsymbol{y} - F(\boldsymbol{x})) + \boldsymbol{c}_1 \tag{2.13}$$

$$-2logP(\boldsymbol{x}) = (\boldsymbol{x} - \boldsymbol{x}_a)^T \boldsymbol{S}_a^{-1}(\boldsymbol{x} - \boldsymbol{x}_a) + \boldsymbol{c}_2 \tag{2.14}$$

where $\boldsymbol{c}_1$ and $\boldsymbol{c}_2$ are constants. Substituting Eq.2.13 and Eq.2.14 in Eq.2.12 we obtain the posterior *pdf*:

$$-2log(P(\boldsymbol{x}|\boldsymbol{y})) = [\boldsymbol{y} - F(\boldsymbol{x})]^T \boldsymbol{S}_\epsilon^{-1}[\boldsymbol{y} - F(\boldsymbol{x})] + [\boldsymbol{x} - \boldsymbol{x}_a]^T \boldsymbol{S}_a^{-1}[\boldsymbol{x} - \boldsymbol{x}_a] + \boldsymbol{c} \tag{2.15}$$

Our inverse problem is ill-posed, with a non-unique solution, so that we have to select the 'optimal' solution from the infinite number of possible ones. One method to find this optimal solution is to maximize the posterior *pdf* $P(\boldsymbol{x}|\boldsymbol{y})$, in this way obtain the most likely state consistent with all of the available information. Alternatively, it could be the solution method which minimizes the error variance when applied to an ensemble of cases. In this particular case the two methods lead to same solution for the state vector, but we will show the second. In this framework, the retrieval $\hat{\boldsymbol{x}}$ is the result of the following operation defined by the *Retrieval Method* $\boldsymbol{R}$: $\hat{\boldsymbol{x}} = \boldsymbol{R}(\boldsymbol{x}_a, \boldsymbol{y}, \hat{\boldsymbol{b}})$ where $\hat{\boldsymbol{b}}$ is the best estimate of the forward model parameters. We want $\boldsymbol{R}$ to produce the Best Linear Unbiased Estimate (BLUE) of the atmospheric state vector $\boldsymbol{x}$. By imposing these three characteristics we can built the function $\boldsymbol{R}$ and find a description of the retrieval error.

For linearity, let's expand $\boldsymbol{R}$, using Taylor expansion with respect to $\boldsymbol{y}$:

$$\hat{\boldsymbol{x}} = \boldsymbol{R}(\boldsymbol{x}_a, \boldsymbol{y}, \hat{\boldsymbol{b}}) + \frac{\partial \boldsymbol{R}}{\partial \boldsymbol{y}}\boldsymbol{\epsilon} + \frac{\partial \boldsymbol{R}}{\partial \boldsymbol{y}}\frac{\partial \boldsymbol{y}}{\partial \boldsymbol{x}}(\boldsymbol{x} - \boldsymbol{x}_a) + O((\boldsymbol{x} - \boldsymbol{x}_a)^2) \tag{2.16}$$

$$\simeq \boldsymbol{R}(\boldsymbol{x}_a) + \boldsymbol{G}\boldsymbol{\epsilon} + \boldsymbol{G}\boldsymbol{K}(\boldsymbol{x} - \boldsymbol{x}_a) \tag{2.17}$$

Where we have defined the gain $\frac{\partial \boldsymbol{R}}{\partial \boldsymbol{y}} = \boldsymbol{G}$, representing the sensitivity of the retrieval to the measurement (the same to measurement error) and $\frac{\partial \boldsymbol{y}}{\partial \boldsymbol{x}} = \boldsymbol{K}$ the Jacobian (the sensitivity of the forward model to the state).

For $\hat{\boldsymbol{x}}$ to be unbiased it is necessary to impose that:

$$\boldsymbol{R}(\boldsymbol{x}_a) = \boldsymbol{x}_a \tag{2.18}$$

Finally, in order to have the minimum variance we need to focus on the error $\hat{\boldsymbol{x}} - \boldsymbol{x}$:

$$\hat{\boldsymbol{x}} - \boldsymbol{x} = \boldsymbol{R}(\boldsymbol{x}_a) + \boldsymbol{G}\boldsymbol{\epsilon} + \boldsymbol{G}\boldsymbol{K}(\boldsymbol{x} - \boldsymbol{x}_a) - \boldsymbol{x} \tag{2.19}$$

Which can be rewritten as, by adding and subtracting $\boldsymbol{x}_a$ and using Eq.2.18:

$$\hat{\boldsymbol{x}} - \boldsymbol{x} = \boldsymbol{G}\boldsymbol{\epsilon} + (\boldsymbol{G}\boldsymbol{K} - \mathbb{I})(\boldsymbol{x} - \boldsymbol{x}_a) \tag{2.20}$$

that allows to divide the error in three components:
- the bias, imposed to 0 in this case (it would be $\boldsymbol{R}(\boldsymbol{x}_a) - \boldsymbol{x}_a$))
- the retrieval error $\boldsymbol{G}\boldsymbol{\epsilon}$ (the error in the retrieval due to the measurement error)
- the smoothing error $\boldsymbol{G}\boldsymbol{K}(\boldsymbol{x} - \boldsymbol{x}_a)$, describing how the information of a profile is smoothed: the more the term $\boldsymbol{G}\boldsymbol{K}$ is close to the identity (in the ideal inverse method this matrix would be the identity), the closer the profile is to the original one.

$\boldsymbol{G}\boldsymbol{K}$ is known as the *averaging kernel matrix* $\boldsymbol{A} = \frac{\partial \hat{\boldsymbol{x}}}{\partial \boldsymbol{x}}$, the sensitivity of the retrieval to the true state. It is a very useful quantity that plays a significant role in descriptions of the information content.The rows of $\boldsymbol{A}$ can be interpreted as smoothing function, that are functions peaking at the appropriate level and with a half-width which is a measure of the spatial resolution of the observing system, thus providing a simple characterization of the relationship between the retrieval and the true state. The averaging kernel also has an area, which is found to be approximately unity at levels where the retrieval is accurate, and in general can be thought of as a rough measure of the fraction of the retrieval that comes from the data, rather than the a priori. The columns of $\boldsymbol{A}$ give the response of the retrieval to a δ-function perturbation in the state vector.

We look now for the expectation value of the error for which $\hat{\boldsymbol{x}} - \boldsymbol{x} \to 0$:

$$var(\hat{\boldsymbol{x}} - \boldsymbol{x}) = \boldsymbol{G}\boldsymbol{S}_\epsilon\boldsymbol{G}^T + (\boldsymbol{G}\boldsymbol{K} - \mathbb{I})\boldsymbol{S}_a(\boldsymbol{G}\boldsymbol{K} - \mathbb{I})^T \tag{2.21}$$

that is the error of the retrieval: $\hat{\boldsymbol{S}}_a = \mathbb{E}[(\hat{\boldsymbol{x}} - \boldsymbol{x})(\hat{\boldsymbol{x}} - \boldsymbol{x})^T]$

We want to find an expression for the matrix $\boldsymbol{G}$ such that the error is minimized: $\frac{\partial \hat{\boldsymbol{S}}_a}{\partial \boldsymbol{G}} = 0$ so that:

$$\frac{\partial \hat{\boldsymbol{S}}_a}{\partial \boldsymbol{G}} = 2(\boldsymbol{G}\boldsymbol{S}_\epsilon - \boldsymbol{K}\boldsymbol{S}_a + \boldsymbol{G}\boldsymbol{K}\boldsymbol{S}_a\boldsymbol{K}^T) = 0 \Longrightarrow \boldsymbol{G} = \boldsymbol{S}_a\boldsymbol{K}^T(\boldsymbol{S}_\epsilon + \boldsymbol{K}\boldsymbol{S}_a\boldsymbol{K}^T)^{-1} \tag{2.22}$$

So that we also have an expression for *averaging kernel* $\boldsymbol{A}$:

$$\boldsymbol{A} = \boldsymbol{G}\boldsymbol{K} = \boldsymbol{S}_a\boldsymbol{K}^T(\boldsymbol{S}_\epsilon + \boldsymbol{K}\boldsymbol{S}_a\boldsymbol{K}^T)^{-1}\boldsymbol{K} \tag{2.23}$$

We now also linearize Eq.2.1:

$$\boldsymbol{y} = F(\boldsymbol{x}) + \boldsymbol{\epsilon} \simeq F(\boldsymbol{x}_a) + \boldsymbol{K}(\boldsymbol{x} - \boldsymbol{x}_a) \Longrightarrow \boldsymbol{K}(\boldsymbol{x} - \boldsymbol{x}_a) = \boldsymbol{y} - F(\boldsymbol{x}_a) \tag{2.24}$$

In the case of radiative transfer, we can assume that the forward model $F(\boldsymbol{x})$ is *moderately linear*, i.e. F behaves in approximately a linear manner for small perturbations. This property is generally guaranteed thanks to presence of exponentials and power laws used within them and the absence of discontinuities [2] and holds when the retrieval is performed for sufficiently small perturbations around the reference state. We can now substitute Eq.2.18, Eq.2.22 and Eq.2.24 in Eq.2.17 and obtain:

$$\hat{\boldsymbol{x}} = \boldsymbol{x}_a + \boldsymbol{S}_a\boldsymbol{K}^T(\boldsymbol{S}_\epsilon + \boldsymbol{K}\boldsymbol{S}_a\boldsymbol{K}^T)^{-1}(\boldsymbol{y} - F(\boldsymbol{x}_a)) \tag{2.25}$$

that can be rewritten, using algebraic relationships, to be more easy to compute:

$$\hat{\boldsymbol{x}} = \boldsymbol{x}_a + (\boldsymbol{S}_a^{-1} + \boldsymbol{K}^T\boldsymbol{S}_\epsilon^{-1}\boldsymbol{K})^{-1}\boldsymbol{K}^T\boldsymbol{S}_\epsilon^{-1}(\boldsymbol{y} - F(\boldsymbol{x}_a)) \tag{2.26}$$

The covariance of the solution can be found by substituting the form for $\boldsymbol{G}$ in Eq.2.22 in Eq.2.21, getting to:

$$\hat{\boldsymbol{S}}_a = \boldsymbol{S}_a - \boldsymbol{S}_a\boldsymbol{K}^T(\boldsymbol{S}_\epsilon + \boldsymbol{K}\boldsymbol{S}_a\boldsymbol{K}^T)^{-1}\boldsymbol{K}\boldsymbol{S}_a \tag{2.27}$$

The algorithm

Eq.2.26 must be solved numerically and given the moderate linearity of F, the Gauss-Newton iteration is a straightforward numerical method for finding the solution:

$$\boldsymbol{x}_{i+1} = \boldsymbol{x}_i + (\boldsymbol{S}_a^{-1} + \boldsymbol{K}_i^T\boldsymbol{S}_\epsilon^{-1}\boldsymbol{K}_i)^{-1}[\boldsymbol{K}_i^T\boldsymbol{S}_\epsilon^{-1}(\boldsymbol{y} - F(\boldsymbol{x}_i)) - \boldsymbol{S}_a^{-1}(\boldsymbol{x}_i - \boldsymbol{x}_a)] \tag{2.28}$$

So, we start the iteration from a first guess $\boldsymbol{x}_0$ (usually $\boldsymbol{x}_0 = \boldsymbol{x}_a$). The forward operator F is used to transform $\boldsymbol{x}_a$ from the state space to the measurement space, resulting in $F(\boldsymbol{x}_a)$. In the next step, the difference between $F(\boldsymbol{x}_a)$ and the observation $\boldsymbol{y}$ is used to make the next guess $\boldsymbol{x}_1$ considering the distance from $\boldsymbol{x}_1$ to $\boldsymbol{x}_a$. This is done by weighting these differences by the measurement uncertainty covariance matrix $\boldsymbol{S}_\epsilon$ and, respectively, the prior state covariance matrix $\boldsymbol{S}_a$. Obtaining $\boldsymbol{x}_1$ requires the inversion of F, which is typically not possible analytically. Therefore, the Jacobian matrix $\boldsymbol{K}$ is used to linearize and invert F. Because $\boldsymbol{K}$ is only an approximation for F around $\boldsymbol{x}_a$, $\boldsymbol{x}_1$ obtained with this process is typically not the solution yet and the process must be repeated until $\boldsymbol{x}$ converges to a stable, optimal solution. Note that $\boldsymbol{K}_i$ depends on $\boldsymbol{x}_i$ used for estimating the Jacobian, which means that $\boldsymbol{K}$ must be recalculated for every iteration step, which might be computationally expensive depending on the lengths of $\boldsymbol{x}$ and $\boldsymbol{y}$. The iteration stops when a convergence criterion is reached.

This algorithm can make the retrieval quite unstable, in particular if the true solution is sufficiently far from the current iteration point, for this reason the *Levenberg-Marquardt Method* is used to regularize the process. The new equation for the iteration, according to this method, is:

$$\boldsymbol{x}_{i+1} = \boldsymbol{x}_i + (\gamma_i \boldsymbol{S}_a^{-1} + \boldsymbol{K}_i^T \boldsymbol{S}_\epsilon^{-1} \boldsymbol{K}_i + \beta_i \mathbb{I})^{-1} (\boldsymbol{K}_i^T \boldsymbol{S}_\epsilon^{-1} [\boldsymbol{y} - F(\boldsymbol{x}_i)] + \gamma_i \boldsymbol{S}_a^{-1} [\boldsymbol{x}_i - \boldsymbol{x}_a]) \quad (2.29)$$

where γ is a scalar parameter called the *inflation factor* that allows the algorithm to reduce the impact of an inaccurate initial guess. It's a factor that changes the relative weight between the prior information and the observation: when $\gamma > 1$ less information comes from the observation with respect to prior (note that if $\gamma = \infty$ the solution would be the prior) and the other way round when $\gamma < 1$. γ can be reduced with each iteration, slowly allowing more information from the observation, greatly stabilizing the retrieval. In this way, the algorithm overcomes a poor first guess, remains constrained and converges. For our retrieval we will start from an inflation factor of 1000 with a decrease of 0.3, so that γ will assume the following values: 1000, 300, 100, 27, 8.1, 2.3 and, finally, 1. We first did an optimization based on the χ^2 values in order to confirm this initial value. The retrieval is not allowed to converge until $\gamma = 1$ [32].

β_i is a scaling coefficient adjusted at each iteration used to ensure numerical stability and convergence. Choosing the right β_i can require a long computation, and for this reason we use a simplified version of Marquardt's strategy [33]: the initial value for β is 0.01, the decrease factor is 0.3 and the increasing factor is 10. At $i+1$-step, if $\chi^2_{i+1} > \chi^2_i$ or the update is non-linear, the algorithm doesn't update and retry the iteration with β incremented. If the step is weakly non-linear, β is kept constant and the *inflation factor* is decreased. Otherwise, if the χ^2 is reducing and the update is linear, we decrease γ and β. Finally, if the value of χ^2 is smaller than the maximum value allowed for convergence (2 in this case), the algorithm checks for the convergence using a criterion based on the χ^2:

$$\frac{\chi^2_{i-1} - \chi^2_i}{max(1, \chi^2_{i-1})} < \frac{1}{k} \quad (2.30)$$

$$\frac{\chi^2_{i-1} - \chi^2_i}{max(1, \chi^2_{i-1})} \geq 0 \quad (2.31)$$

where $k = 100$ is the convergence factor. We set 15 as the maximum number of iteration, meaning that if this criterion is not satisfied in this number of steps, the convergence is not reached. The χ^2 used in the convergence test is not computed using the typical formula for this parameter, the generalized definition is used instead:

$$\chi^2 = \frac{(\boldsymbol{x} - \boldsymbol{x}_a)^T \boldsymbol{S}_a^{-1} (\boldsymbol{x} - \boldsymbol{x}_a) + (\boldsymbol{y} - \boldsymbol{y}_m)^T \boldsymbol{S}_\epsilon^{-1} (\boldsymbol{y} - \boldsymbol{y}_m)}{len(y)} \quad (2.32)$$

For this reason it is important to stress that the expected χ^2 value is unknown, especially because the true value of $\boldsymbol{x}$ and $\boldsymbol{S}_\epsilon$ are not known.

The algorithm used introduces other constraints, as the one used to force the physical parameters contained in the state vector to be strictly non-negative. Gases concentration and cloud/aerosol parameters are mapped to an unbounded space via a log-normal distribution, ensuring Gaussian-like behaviour in the new transformed variable while preserving positivity during the optimization process. This choice is also motivated by the fact that, in ill-posed inverse problems such as this one, the solution is not guaranteed to remain within physically admissible bounds. In particular, variables such as water vapour and trace gases can vary over several orders of magnitude, which increases the probability that unconstrained optimization may mathematically converge to negative values. While such solutions may be acceptable from a purely numerical perspective, they are clearly non-physical. The logarithmic transformation therefore stabilizes the retrieval and enforces physical consistency.

A similar transformation is applied to the component of the aerosol state vector. For the aerosol content c_a, the transformed variable is defined as:

$$\tilde{x}_{a,c} = log(\frac{c_a}{c_2})$$

For the aerosol particle radius r_a, the transformation is defined as:

$$\tilde{x}_{a,r} = log(\frac{r_a - c_r}{c_1})$$

where c_1 and c_2 are scaling constants introduced to adimensionalise the variables and c_r acts as a lower bound constraint on the radius. In our implementation, c_r is set to 0.03 μm, which defines the minimum admissible radius within the retrieval framework. We took this value as the lower limit because in the SAF [34] products from which we will take the statistics the lowest dust radius range starts from this value. A similar approach is used to constrain emissivity in the [0,1] interval, using a logit transformation.

So, the forward model relates the transformed state to spectral radiance measurement as:

$$\boldsymbol{y} = F(exp(\tilde{\boldsymbol{x}}_1), logit(\tilde{\boldsymbol{x}}_\mathbf{2}), \boldsymbol{x}_3)) + \boldsymbol{\epsilon}$$

Where $\tilde{\boldsymbol{x}}_1 = log(\boldsymbol{x}_1)$ and $\tilde{\boldsymbol{x}}_2 = logistic(\boldsymbol{x}_2)$ are the variables of the state vector that are transformed while $\boldsymbol{x}$ are the components for which no transformation is applied (temperature profiles and surface temperature).

Principal component analysis and dimensionality reduction

Another issue with the inversion problem is due to the high dimensionality of the state vector $\boldsymbol{x}$; to reduce the dimensionality a principal components (PCs) decomposition

of the variables is done [35]. Principal component analysis is a linear dimensionality reduction technique in which data are linearly transformed onto a new coordinate system such that the directions (principal components) of the new base capture the largest variation in the data, so that the computational cost is reduced while preserving the main features of the original state. So, we look for an algebraic description that simplifies our problem and well-expresses the data. To that, we focus on two characteristics of data: noise and redundancy.

Every measurement is affected by noise, which affects the amount of information one can extract from the signal. A measure of this quantity is the signal-to-noise ratio (SNR). We can assume that the directions with largest variances (and high SNR) in measurement space contain the dynamics of interest so that by maximizing the variance we can find the new base that best represents our data.

Another central idea behind the dimensional reduction is that data can be redundant, meaning that having many data does not necessarily mean that we can extract many information. So the idea is that we want to get rid of redundant data (i. e. reduce the dimensionality) without losing important information.

The covariance matrix, which is the measure of the degree of the linear relationship between variables, reflects redundancy and noise in the measurement. The diagonal terms of the covariance matrix represent the variance of a measurement while the off-diagonal terms represent the covariance between measurements. So, the values in the diagonal correspond to the interesting features of the variable that we want to extract and the off-diagonal terms correspond to the redundancy that we want to minimize. In this framework we can understand how to find the new base: the one in which the covariance matrix is diagonal.

In our case, we use the *singular value decomposition (SVD)* method to find the change of bases, according to which we can rewrite an arbitrary $n \times m$ $\boldsymbol{X}$ matrix in this way:

$$\boldsymbol{X} = \boldsymbol{U}\boldsymbol{\Sigma}\boldsymbol{V}^T$$

where:

- $\boldsymbol{V} = [\hat{\boldsymbol{v}}_1\, \hat{\boldsymbol{v}}_2 \ldots \hat{\boldsymbol{v}}_r]$ is the matrix made with the set of *orthonormal* $m \times 1$ eigenvectors with associated eigenvalues $\{\lambda_1, \lambda_2, ..., \lambda_r\}$ for the symmetric $m \times m$ matrix $\boldsymbol{X}^T\boldsymbol{X}$ of rank r. The columns of $\boldsymbol{V}$ are the right singular vector of $\boldsymbol{X}$

- $\boldsymbol{U} = [\hat{\boldsymbol{u}}_1\, \hat{\boldsymbol{u}}_2 \ldots \hat{\boldsymbol{u}}_r]$ is the matrix made with set of $n \times 1$ vectors defined as: $\hat{\boldsymbol{u}}_i \equiv \frac{1}{\sigma_i}\boldsymbol{X}\hat{\boldsymbol{v}}_i$ where $\sigma_i = \sqrt{\lambda_i}$ are the *singular values*. So, the columns of $\boldsymbol{U}$ are the left singular vector of $\boldsymbol{X}$

- $\boldsymbol{\Sigma}$ is the diagonal matrix where the diagonal terms are the *singular values* in decreasing order. By substituting $\boldsymbol{X}$ with the symmetric covariance matrix $\boldsymbol{S}_a$, and considering

that, due to its symmetry, $\boldsymbol{U} = \boldsymbol{V}$ (left and right singular vectors are the same), we can decompose the covariance matrix in this way:

$$\boldsymbol{S}_a = \boldsymbol{V}\boldsymbol{\Sigma}_a\boldsymbol{V}^T$$

For dimensionality reduction, we can use a truncated version of the singular value decomposition by selecting the first q largest singular values in $\boldsymbol{\Sigma}$. In this way we can project the prior offset $\boldsymbol{x} - \boldsymbol{x_a}$according to this decomposition as:

$$\boldsymbol{z}_q = \boldsymbol{V}_q^T(\boldsymbol{x} - \boldsymbol{x_a})$$

where $\boldsymbol{V}_q$ is a $r \times q$ matrix with the first q eigenvectors (with $q < m$). q, the number of principal components must be chosen so that we can capture the majority of the variance. In particular, the number of principal components is selected according by defining the *compression error* as [31]:

$$\boldsymbol{\epsilon}_c = \boldsymbol{K}(\mathbb{I} - \boldsymbol{V}\boldsymbol{V}^T)(\boldsymbol{x} - \boldsymbol{x}_a)$$

and considering the minimum number of principal components such that: $\boldsymbol{\epsilon}_c << \boldsymbol{\epsilon}$.

So, the algorithm described earlier is not applied directly to the state vector $\boldsymbol{x}$ but on $\boldsymbol{z}$, and Eq.2.29 is actually solved as:

$$\boldsymbol{z}_{i+1} = \boldsymbol{z}_i + (\gamma_i\boldsymbol{\Sigma}_a^{-1} + \tilde{\boldsymbol{K}}_i^T\boldsymbol{S}_\epsilon^{-1}\tilde{\boldsymbol{K}}_i + \beta_i\mathbb{I})^{-1}(\tilde{\boldsymbol{K}}_i^T\boldsymbol{S}_\epsilon^{-1}[\boldsymbol{y} - \tilde{F}(\boldsymbol{z}_i)] + \gamma_i\boldsymbol{\Sigma}_a^{-1}[\boldsymbol{z}_i]) \quad (2.33)$$

with $\tilde{F}(\boldsymbol{z}_i) = F(\boldsymbol{V}\boldsymbol{z}_i + \boldsymbol{x}_a)$ and $\tilde{\boldsymbol{K}} = \boldsymbol{K}\boldsymbol{V}$. When the algorithm converges, the solution $\boldsymbol{z}$ is transformed in the physical state in order to obtain the optimal estimation of the state vector $\hat{\boldsymbol{x}}$:

$$\hat{\boldsymbol{x}} = \boldsymbol{V}\hat{\boldsymbol{z}} + \boldsymbol{x}_a \quad (2.34)$$

Similarly, starting from Eq.2.27 the error covariance matrix is calculated as:

$$\hat{\boldsymbol{S}}_{\boldsymbol{x}} = (\tilde{\boldsymbol{G}}\boldsymbol{K} - \mathbf{I})\boldsymbol{S}_a(\tilde{\boldsymbol{G}}\boldsymbol{K} - \mathbf{I})^T + \tilde{\boldsymbol{G}}\boldsymbol{S}_\epsilon\tilde{\boldsymbol{G}}^T \quad (2.35)$$

the gain G from Eq.2.22:

$$\tilde{\boldsymbol{G}} = \boldsymbol{V}(\gamma_i\boldsymbol{\Sigma}_a^{-1} + \tilde{\boldsymbol{K}}_i^T\boldsymbol{S}_\epsilon^{-1}\tilde{\boldsymbol{K}}_i)^{-1}\tilde{\boldsymbol{K}}_i^T\boldsymbol{S}_\epsilon^{-1} \quad (2.36)$$

and the *averaging kernel* is

$$\tilde{\boldsymbol{A}} = \tilde{\boldsymbol{G}}\boldsymbol{K} \quad (2.37)$$

2.2.1 Validation

Once the retrieval of the atmospheric state is completed, the results must be validated to confirm that the retrieved quantities are as accurate as is possible, and that their

relationship to the true state is properly understood. In this general sense, validation aims to verify the theoretical and instrumental assumptions of the measurement system. Discrepancies identified at this stage may arise either from deviations of the instrument from its nominal performance or from limitations in the retrieval methodology. The testing and validation procedure includes elements such as: a full error analysis and characterization of the observing system, an internal consistency checks, comparison of the measured signals with independent direct measurements of the profile, retrieval validity test such as a χ^2 test, comparison of the retrievals with the a priori [31].

2.3 Aerosol

Atmospheric aerosols are colloidal systems of liquid or solid particles suspended in the atmosphere. There are many different types of aerosols, that can differ in size, origin and composition. Their dimension can range from a few tens of nanometers to several tens of micrometers; they can be directly injected into the atmosphere, in this case are known as 'primary aerosols', or can be emitted in another form (e.g. gases), then become aerosol particles after going through chemical reactions in the atmosphere ('secondary aerosol'). The sources of these particles is usually classified as natural or anthropogenic (related to human activities). Natural aerosol can be particles such as like mineral dust, sea-salt, smoke or volcanic ash; while anthropogenic aerosol can be sulfites, black carbon or organic carbon compounds.

Atmospheric aerosols play a significant and complex role in Earth's weather, climate and in human health [36]. Because different types of particles have different effects, aerosols are a hot topic in climate research. Their impact on climate is both direct and indirect. The direct effect is a radiative one, as they interact with incoming and outgoing radiation. Depending on their optical, physical and chemical properties, particles can either scatter or absorb radiation, interfering with the Earth's radiative budget. For some types of aerosol scattering processes of the solar incoming radiation are predominant, leading to a cooling effect. In contrast, absorbing aerosol like black carbon absorb solar radiation and warm the atmosphere. The indirect effects of aerosol on climate mainly depend on their influence on cloud properties and precipitation processes. These particles act as condensation and ice nuclei so they partly determine the microphysical and radiative properties of clouds, by influencing their optical properties, cloud cover, cloud lifetime and precipitation. There are many uncertainties related to the study of aerosol and it is still quite difficult to assess its exact role [10]. For these reasons, it is essential to estimate the chemical and physical properties of aerosol in order to be able to predict and understand their impact.

Desert dust aerosols are the most prominent tropospheric aerosol, they are emitted when wind blows over deserts or otherwise dry soils, lifting the particles get carried off into the atmosphere [37]. Mineral dust aerosols strongly affect the radiative budget at local, regional and global scale via scattering and absorption of both solar and infrared radiation. The capacity of dust to interact with radiation throughout the atmospheric spectrum is due to its extended size distribution, including particles from hundreds of nanometres to several tenths of micrometres and its mineralogical composition, including silicates, carbonates and iron oxides showing multiple absorption bands across the shortwave to infrared spectral range. In particular, strong infrared absorption is identified due to the resonance peaks of quartz, clays (illite, kaolinite, smectite), and calcite. The absorption in the infrared contributes to a positive dust direct radiative effect at top of the atmosphere, which opposes and counteracts a significant part of the dust negative radiative effect resulting from the dominant scattering at solar wavelengths [38].

However, their radiative forcing is still not known with sufficient precision to determine its sign and in recent years a growing effort has been devoted to improving the knowledge of dust characteristics. The sources of uncertainty are multiple, one of them being a poor characterisation of the dust aerosol's vertical profile on a global scale. Due to the limited number and uneven distribution of ground-based observation stations, obtaining comprehensive information on the sources and transportation of dust aerosols is challenging. Satellite remote sensing has emerged as an ideal tool for studying the spatial–temporal distribution and transport characteristics of dust aerosols. The mainstream methods for satellite dust identification can be classified into four categories: visible light–near-infrared, ultraviolet, thermal infrared, and passive microwave. The currently most advanced aerosol retrievals from satellite sensors are based on UV, visible or near-infrared wavelengths. Shortwave reflectance observations are widely used but they are highly uncertain over deserts due to the influence of surface reflection and they are limited to the daytime. Retrievals of aerosol long-wave optical properties are less well developed but have received great attention these last years. Thermal infrared observations are mainly influenced by slowly varying factors such as atmospheric temperature profiles, surface temperature, and surface emissivity, which is conducive to the quantitative inversion of dust aerosols over high-reflectance surfaces during nighttime [20]. Moreover, in the thermal infrared, mineral dust exhibits distinctive spectral absorption and emission features associated with its composition and particle size, enabling the retrieval of dust optical depth and providing sensitivity to the coarse aerosol mode. Brightness temperature differences across multiple infrared channels can also be exploited to infer information on dust layer altitude and effective

particle size. These characteristics make infrared observations particularly valuable for the detection and characterization of desert dust and other coarse aerosols, complementing shortwave-based retrievals and extending aerosol monitoring capabilities to both day and night conditions.

Chapter 3

Data

The retrieval framework described in Chapter 2 requires multiple input datasets and independent observations for validation. This chapter describes the datasets used in this study and the preprocessing steps applied prior to their integration into the inversion system.

3.1 Radiosonde

Radiosonde data are used as the reference dataset for the validation of the inversion model. They are considered the most accurate data available for atmospheric profiles, as they are collected in situ. The radiosonde measurements used in this study come from the station located in San Pietro Capofiume (BO), shown in Fig.3.1. Atmospheric radiosondes provide information on the vertical profiles of temperature, relative humidity, dew-point temperature, and wind speed and direction at a series of pressure levels, from the surface up to an average altitude of about 25 km. In this work, we focus exclusively on temperature and relative humidity data. Radiosonde launches are carried out daily at 00:00 UTC and 12:00 UTC (Greenwich Mean Time). The measurements are performed by a radiosonde carried upward by a helium-filled balloon, with data transmitted every 2 seconds via a radio link to the ground receiving station. Radiosonde data provide the most accurate measurements available of temperature and humidity variables. For this reason, in addition to being used for analyses of the thermodynamic structure of the atmosphere, they are employed to generate initial-condition analyses for weather forecasting and to validate inversion models [24].

Radiosonde data are downloaded from the website [39], using the San Pietro Capofiume station code 16144, from which all data corresponding to the year 2023 are retrieved. The atmospheric profiles provided by these radiosonde measurements extend up to a pressure of 100 hPa; therefore, it is necessary to complete the missing upper-

atmosphere portion by merging them with the IG2 climatological profiles. IG2 profiles are climatological profiles defined for different latitude bands, seasons, and times of day. In our case, we use the data for the mid-latitudes of the Northern Hemisphere, selecting the season and day/night conditions according to the month and the time of the radiosonde launch. The merging of the two profiles is performed by dividing the atmosphere into three pressure ranges: the lower atmosphere (up to 250 hPa), a transition zone from 250 hPa to 100 hPa, and the upper atmosphere. In the lower range, radiosonde data are used; in the upper range, climatological data are applied, while in the transition zone the two profiles are blended through a weighted average. During the merging process, the data are also cleaned to remove any potential anomalies. We will compare these measurements with retrieved temperature and humidity profiles, which are defined on the 60-levels σ pressure grid, and so, we need to interpolate the radiosonde data onto the σ-grid. To do that, we first perform a linear interpolation on the 60-levels grid. A combined grid is then defined, consisting of both the original radiosonde pressure levels (with their corresponding temperature and humidity data) and the σ pressure levels (with the interpolated data). Finally, a weighted average between the original and the interpolated data is applied based on the distance from each point on the σ-grid. Interpolated data of humidity and temperature are shown in Fig.3.2, up to 100 hPa, since above this level the profiles become identical due to the transition to the climatological values.

The temporal coverage of these measurements is not complete as many days in March, April and May are not available. Retrieval corresponding to missing days are still performed but not compared with the ground-based measurement.

Overall, we therefore obtain temperature and relative humidity profiles available for the most part of 2023, covering the full atmosphere and aligned with the same vertical pressure coordinates used by σ.

These data can have several applications: they can be used for comparison with IASI Level 2 data, as the initial guess in the retrieval and, finally, our focus here, as validation of the retrieval algorithm by comparing them with the inversion results.

3.2 IASI Satellite

Radiance data are obtained from IASI (Infrared Atmospheric Sounding Interferometer) measurements, an instrument capable of providing emission spectra with very high accuracy and resolution, used to derive profiles of various atmospheric variables. It is mounted on the MetOp satellite in polar orbit, which is part of the EUMETSAT Polar System (EPS) segment, providing data for weather forecasting and climatological mon-

Figure 3.1: *Location of the radiosonde base (white circle) (latitude = 44.65°, longitude = 11.6°) with respect to Bologna*

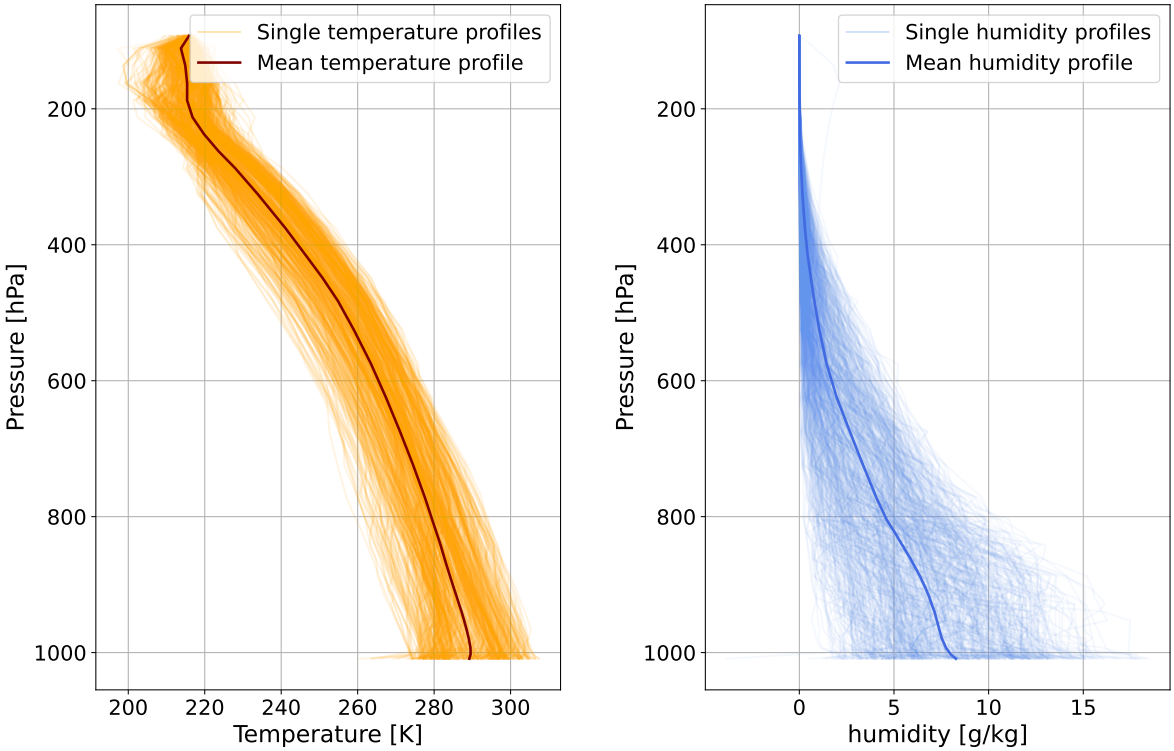

Figure 3.2: *Temperature (left panel) and humidity (right panel) data from the radiosonde measurements, interpolated on the σ pressure grid, shown up to 100 hPa. Single profiles and mean profile are shown*

itoring. IASI has flown on MetOp-A, -B, and -C since 2006, providing continuous global coverage twice per day. IASI is a Fourier transform spectrometer based on a Michelson interferometer, coupled with an integrated imaging system that observes and measures the infrared radiation emitted by the Earth. The optical interferometry process enables very fine spectral sampling of the atmosphere in the infrared band. IASI covers 8461 spectral channels across the infrared range ($[645 - 2760]$ cm^{-1}), for wavelengths between 3.4 μm and 15.5 μm. This allows the instrument to determine temperature and water vapor profiles in the troposphere and lower stratosphere, as well as to measure concentrations of ozone, carbon monoxide, methane, and other compounds, which are of fundamental importance in atmospheric processes. The IASI interferometer's field of view is square, observed at an angle of $3.33° \times 3.33°$, corresponding to approximately 50×50 km at nadir. Each cell is simultaneously observed by a 2×2 array of detectors, each with a viewing angle of 1.25°. At nadir, the instrument samples data at 12 km intervals along-track and cross-track, so each sampling has a maximum footprint of 12 km. The across-track swath extends to $\pm 48,3°$ from nadir, corresponding to 30 detector positions, corresponding to a swath on the ground of $\sim$ 2000 km [1].

We will use two IASI products: Level 1c data and Level 2 data.

3.2.1 Level 1C

IASI Level 1c data are geolocated, calibrated, and apodized radiances. They contain infrared radiance spectra at a spectral resolution of 0.25 cm^{-1}. For each pixel, the product contains 8461 spectral samples covering a wavenumber range from 645 cm^{-1} to 2760 cm^{-1}. In addition to the radiances, Level 1c data include other measurements parameters, such as the solar and satellite zenith and azimuth angles, as well as the fraction of cloud cover and land present in each pixel. Scaling factors required to correctly rescale the radiance measurements are also provided. Data are downloaded through the EUMETSAT portal, where it is possible to select the time period and geographic area of interest. For this work, data from 2023 near San Pietro Capofiume (BO), in the Po Valley, are retrieved. Entire orbits are downloaded, from which only the data relevant to the study are extracted. Specifically, radiance data sufficiently close to the location of interest at San Pietro Capofiume (latitude = 44.65, longitude = 11.6) are selected, discarding all pixels farther than 12 km. The satellite overpass time over the region of interest is distributed into two distinct time windows: one in the morning (around 08:00–10:00 UTC) and one in the late afternoon–evening (around 17:00–19:00 UTC). It can therefore be noted that the IASI overpass times do not coincide with the radiosonde launch time (00:00 UTC and 12:00 UTC). In the following analysis the inversions (both the clear-sky and the aerosol ones) are performed only for cases

classified as clear-sky conditions according to the Level 2 parameters. To perform this selection, that is explained in the next section, a parameter available in Level 2 data is considered [18]. Finally, the measured IASI radiances are rescaled using the provided scaling factors and converted to the appropriate units for input into σ, i.e., from $W/(m^2\, sr\, m^{-1})$ to $mW/(m^2\, sr\, cm^{-1})$,

At the end of this processing, we thus obtain the 2023 radiance measurements for pixels near our point of interest, classified as clear-sky conditions, ready to be input into the inversion model. In addition to the radiances, also the zenith angle, necessary for the inversions, will be extracted from each measurement.

The error associated with the IASI observations is provided by EUMETSAT. In particular, we inflate the observation covariance matrix by a factor of 2 to account for additional forward-model and representation errors not included in the instrumental noise, and to partially account for possible correlations between measurement errors that are not explicitly represented in the covariance matrix.

As an example, Fig.3.3 and Fig.3.4 show IASI radiance measurements over the area of interest for four days: two in January and two in June, under clear-sky and cloudy-day conditions. The corresponding brightness temperatures are shown in Fig.3.5 and Fig.3.6.

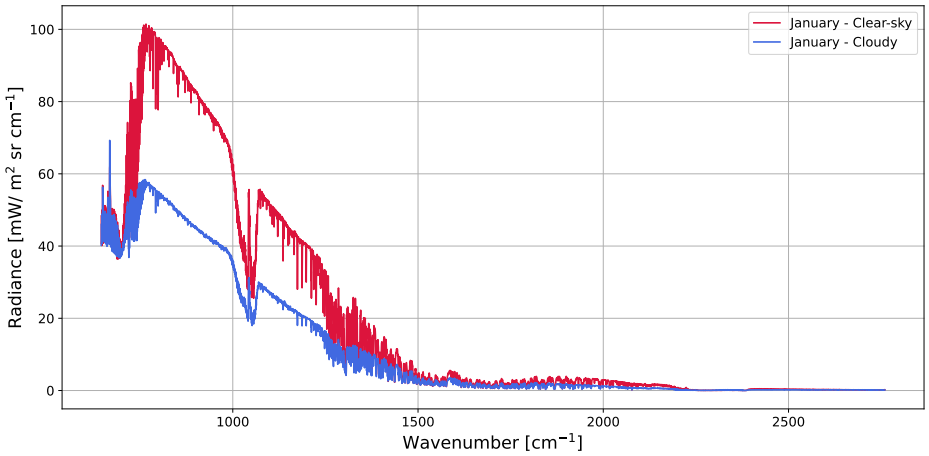

Figure 3.3: *IASI radiance measurements for two days in January 2023: one clear-sky (red line) case and one cloudy case (blue line).*

3.2.2 Level 2

IASI Level 2 data include humidity and temperature profiles with vertical accuracies of approximately 1K and 10% per 1-km layer respectively, as well as surface pressure, surface emissivity, trace gases, and the cloud cleared radiances on a global scale. These products are available to the operational user community. As with Level 1 data, they

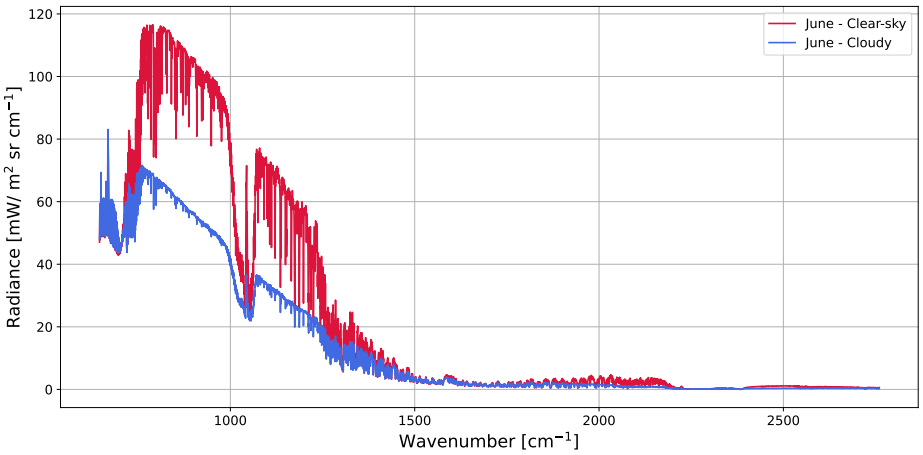

Figure 3.4: *IASI radiance measurements for two days in June 2023: one clear-sky (red line) case and one cloudy case (blue line).*

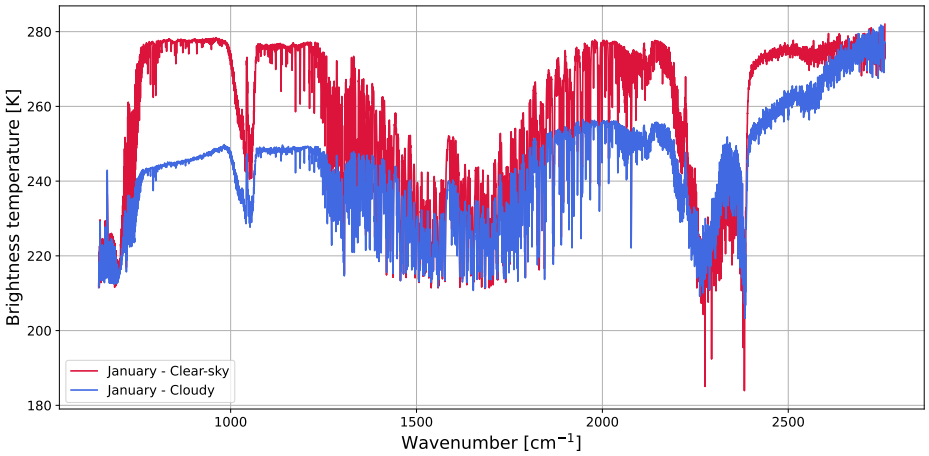

Figure 3.5: *Brightness temperature from IASI measurements for two days in January 2023: one clear-sky (red line) case and one cloudy case (blue line).*

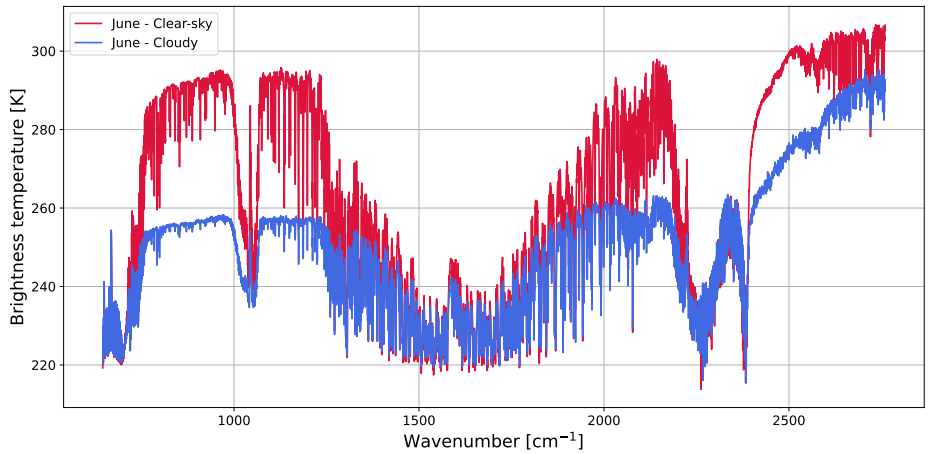

Figure 3.6: *Brightness temperature from IASI measurements for two days in June 2023: one clear-sky (red line) case and one cloudy case (blue line).*

are downloaded from the EUMETSAT portal and geographically selected according to the region of interest.

Among the parameters available in this dataset, we are interested in the cloud detection products, that are performed with three concurrent cloud detection methods using Advanced Very High Resolution Radiometer (AVHRR) collocated cloud mask, the Numerical Weather Prediction (NWP) forecasts and IASI measurements. The AVHRR is a six-channel imaging and scanning radiometer performing several tests combining its measurements in order to evaluate the homogeneity of the scenes. In the NWP test window channels radiances simulated with weather forecasts and are compared to the actual IASI observations in these channels; large differences indicate the presence of a cloud in the IASI field of view. The third test applies artificial neural networks to IASI radiances and AVHRR cluster information to classify the scenes into cloud-free; partly cloudy and fully cloudy. For each method a test is applied, and if all tests conclude that there is an absence of clouds, the instantaneous field of view is declared cloud-free with high confidence. The results of the tests are summarized in the parameter *flag_cldnes* according to which four categories of cloudiness are assigned to each pixel. The categories are: clear with high confidence, (*flag_cldnes* = 1), presumably clear (*flag_cldnes* = 2), partly cloudy (*flag_cldnes* = 3) and cloudy (*flag_cldnes* = 4). For the first two scenarios, an Optimal Estimation retrieval is performed and L2 data of temperature, humidity and ozone profiles are given. We will perform the retrieval for the same measurements for which an L2 data product is available. In all the other cases, the OE retrieval is not performed and the products are given by a Piece-Wise Linear Regression-cube (PWLR3) algorithm, which provides estimates of the temperature, water-vapour and ozone profiles in all-sky conditions as well as surface skin temperature and surface emissivity. The PWLR3 retrievals serve as "first guess" to the Optimal Estimation method used in clear-sky retrievals.

Another useful parameter provided in L2 data is the dust index; a unitless indicator providing a pseudo-quantitative information of the dust load in the IASI pixels. As such, it is not a physical quantitative characterisation of the dust content and nature. The values typically range between 0 and 10, can reach higher values in exceptional dust outbreaks. The presence of dust is suspected when the index is greater than approximately 2. The dust index can be read from the flag *flg_dustcld* [7]. The algorithm producing the Dust Flag was developed by L. Clarisse and identifies five distinct aerosol types using the brightness temperature difference technique. The retrieved categories are volcanic ash, sulfuric acid droplets, ammonium sulfate particles, smoke particles, and windblown dust. The presence of a particular aerosol type is suspected by calculating the radiative temperature difference (ΔBT) at selected wavelengths. In the case

of mineral dust, 3.7 and 11 μm were selected. Dust presence is strengthened for large values of $\Delta BT = BT_{3.7\mu m} - BT_{11\mu m}$. The final product is calculated from the following equation:

$$dust\_index = \sum_{i=0}^{n_dust} G_i[r(ch_i - m_i)] - bias \tag{3.1}$$

where G is the gain matrix, which determines the sensitivity of the final product to each wavelength, r is the satellite radiation measurement, ch_i are the different wavelength channels selected for retrieving dust information, *bias* is a calibration offset, and m_i are the background reference spectrum [40].

In addition to the information on clouds and aerosols, we will extract surface pressure values, which are necessary in the inversion model for the retrieval but are not provided by Level 1 data.

Furthermore, Level 2 data can also be used for comparison with radiosonde measurements and with the results of the inversions themselves, after they have been correctly interpolated onto the σ pressure grid.

3.3 ERA5

ERA5 represents the fifth generation of atmospheric reanalyses from the European Centre for Medium-Range Weather Forecasts (ECMWF), covering the period from January 1940 to the present. It provides a large number of atmospheric, surface, and oceanic variables. The data cover the Earth's surface with a horizontal resolution of 31 km and are provided on 137 vertical levels, from the surface up to 80 km [41]. ERA5 data for 2020, 2021, 2022 are downloaded, selecting the Po Valley as the geographical region of interest. Data corresponding to time windows around the IASI overpass times over the region of interest were therefore downloaded. These data are used to compute the statistics for the *a priori*. In particular, the variables considered are: temperature and humidity profiles, ozone, water and ice content, as well as surface temperature and pressure. From the humidity profiles the HDO profiles are calculated using the following formula:

$$HDO = \frac{m_{air}}{m_{H2O}} \cdot q \cdot 3.1 \times 10^{-7}$$

where $m_{air} = 28.96$ $[g/mol]$ and $m_{water} = 18.015$ $[g/mol]$ are the molar masses of air and water and $3.1{\times}10^{-7}$ is the assumed atmospheric isotopic ratio between HDO and H_2O

The downloaded data are provided on 137 *model levels*, so as a first step it is necessary to calculate the corresponding pressure values at these levels, as described in [42]. From the surface pressure (p_surf) we compute the model half-level pressure

(*press_half*) of each layer with this formula:

$$press\_half = A + B \cdot p\_surf$$

from which we can compute the pressure (p_ml) on the *model levels*:

$$p_{ml} = \frac{p\_half\_above + p\_half\_below}{2}$$

A and B are tabulated coefficients defining the *model levels* [43]. Subsequently, it is necessary to map the pressure levels onto those used by σ, since these data will be used as input for the inversion model. This is done by performing a linear interpolation, in a similar way as was done for the radiosonde data.

3.4 Prior distributions

In this section, data and the methodology used to construct the prior is described.

T, H_2O, HDO, T_{sup}, O_3

To build the *a priori* (mean and covariance) for temperature, humidity, surface temperature and ozone ERA5 data are used. The prior should represent the typical state of the atmosphere in the region, season, and time of the measurements. For this reason, we selected data from the Po Valley during a period close to that of interest (2020-2022). These choices are based on the assumption that, by selecting data from the same geographical region and from a period close to that of interest, we are considering similar dynamical structures and comparable meteorological patterns. In this way, we assume that the dominant physical processes governing temperature, humidity, surface temperature and ozone are analogous to those occurring at the time of the measurements. This approach allows us to better capture the natural variability of these variables at the point of interest and to construct a prior that is physically consistent with the atmospheric conditions we aim to represent.

When only clear-sky retrieval are performed is therefore necessary to consider cloud-free conditions when creating the prior. Clear-sky points are selected by considering the total optical depth (OD) at 900 cm^{-1} of each pixel, using humidity, water content, and ice content. Calculating OD requires temperature, humidity, pressure, water and ice content and their optical properties. We first compute the height D of each layer with the hypsometric equation, the efficient radius and extract the extinction coefficients. We used the following equation to compute the efficient radius of water droplets:

$$r_{e,w} = \left(\frac{3LWC}{4\pi \cdot \rho_w \cdot k \cdot Nd} \right)^{\frac{1}{3}}$$

Where LWC is the liquid water content, ρ_w the the density of water, k a characteristic parameter of the drop size distribution, set to 0.69 over land and Nd the total number of cloud droplets. The efficient radius of ice cloud is computed using the following equation:

$$r_{e,i} = \frac{3\sqrt{3}}{8} D_e^{ice}$$

where D_e^{ice} is parametrized as follows :
$D_e^{ice} = 1.2351 + 0.0105(T - 273.15)(a + b(T - 83.15))$
with : $a = 45.8966\, IWC^{0.2214}$, $b = 0.7957\, IWC^{0.2535}$
IWC is the ice water content.

Extinction coefficients Q_{ext} are extracted from the spectroscopical database containing single scattering properties for Scattnlay smooth water spheres [27] and single scattering properties for Ping Yang smooth aggregate columns [29]. OD of a layer of height D is then calculated as:

$$OD_{w,i} = \frac{3 w_{w,i} \rho_{air} Q_{ext} D}{4 r_{e_{w,i}} \rho_{w,i}}$$

where $w_{w,i}$ is the mixing ratio of water and ice. Now the total optical depth can be found by adding the ODs of all the layers, relative to ice and water [44]. If the condition $OD < 0.003$ is satisfied the pixel is classified as clear sky and used to construct the prior.

Thus, using these clear-sky data mapped to the σ pressure levels, statistical analyses are performed. In particular, the mean and covariance matrix are calculated for the following variables: temperature, humidity, ozone and heavy water, as well as the mean and variance of surface temperature. Since the logarithmic transformation is performed by the inversion algorithm for humidity, heavy water and ozone, for these variables the logarithmic statistics are computed. In particular, for the covariance matrix a Taylor expansion is needed:

$$S_{log} = \frac{1}{x_{mean}} \cdot S \cdot \frac{1}{x_{mean}}$$

Where S is the covariance matrix, and $\frac{1}{x_{mean}}$ is a diagonal matrix made with the inverse of the mean vector.

A Gaussian filter with $\sigma = 0.5$ is applied to the covariance matrix of humidity and heavy water. To compute the statistics, only the profiles that reach a surface pressure greater than 1005 hPa are considered, so that they cover all the 60 σ pressure levels.

The statistics are computed by grouping the data into two six-month seasons (the summer season from the fourth to the ninth month, and the remaining months for the winter season), ensuring that for each season there are at least 61 valid profiles available. This guarantees ensures sufficient sampling to avoid rank deficiency, which is optimal for the inversion.

Mean temperature, humidity and ozone profiles used as prior and first guess are shown in Fig.3.7 and relative covariances in Fig.3.8.

Regarding the surface temperature, the use of the 6 months mean represents an overly coarse approximation and, given its importance in the retrieval process, may lead to inaccurate results. Therefore, instead of adopting the mean value derived from these statistics, the surface temperature will be estimated during the retrieval process by computing the brightness temperature at 900 cm^{-1} (averaging over 10 spectral points around this wavenumber) for each retrieval.

A first comparison that can be performed to assess the suitability of our chosen prior consists in comparing the mean temperature and humidity profiles with those derived from the radiosonde observations, which will later serve as the reference for the evaluation of the retrieval results. In this way, we obtain an initial qualitative assessment of how well our a prior distributions represent what can be considered the true state of the atmosphere. The results are shown in Fig.3.9. Regarding temperature in the cold month, we find a good agreement in the values, both profiles show the typical temperature inversion near the surface. In the warm months, however, the radiosonde temperatures are higher than those of the prior by approximately 3 K. This difference gradually decreases toward the upper troposphere. For humidity, the radiosonde values are higher than those of the prior in both warm and cold months. The difference amounts to about 2 g/kg in the cold season and approximately 4 g/kg in the warm season. These differences vanish in the upper troposphere, where both datasets approach nearly zero values.

Emissivity, CO_2 and CH_4

Prior distribution for emissivity are calculated from the Huang research group dataset [45], that contains global data of surface spectral emissivity. In particular, we used the nadir-view spectral emissivity at a $1cm^{-1}$ resolution for the entire long-wave spectrum, used for remote sensing application. We selected as region of interest all the points closer than 200 km from the radiosonde location and we computed the mean for the cold and warm months. Before calculating the statistics, the logit function is applied to each data to constrain emissivity in the [0,1] interval. As variance, we used vector of ones, as the variability of the dataset was too low and the variance computed from the dataset led to numerical instability.

In order to have more realistic profiles for CO_2 and CH_4 a correction factor is introduced by comparing the concentration near to surface with the value provided by the Integrated Carbon Observation System (ICOS) [46]. ICOS is a European-wide greenhouse gas research infrastructure, it produces standardised data on greenhouse gas

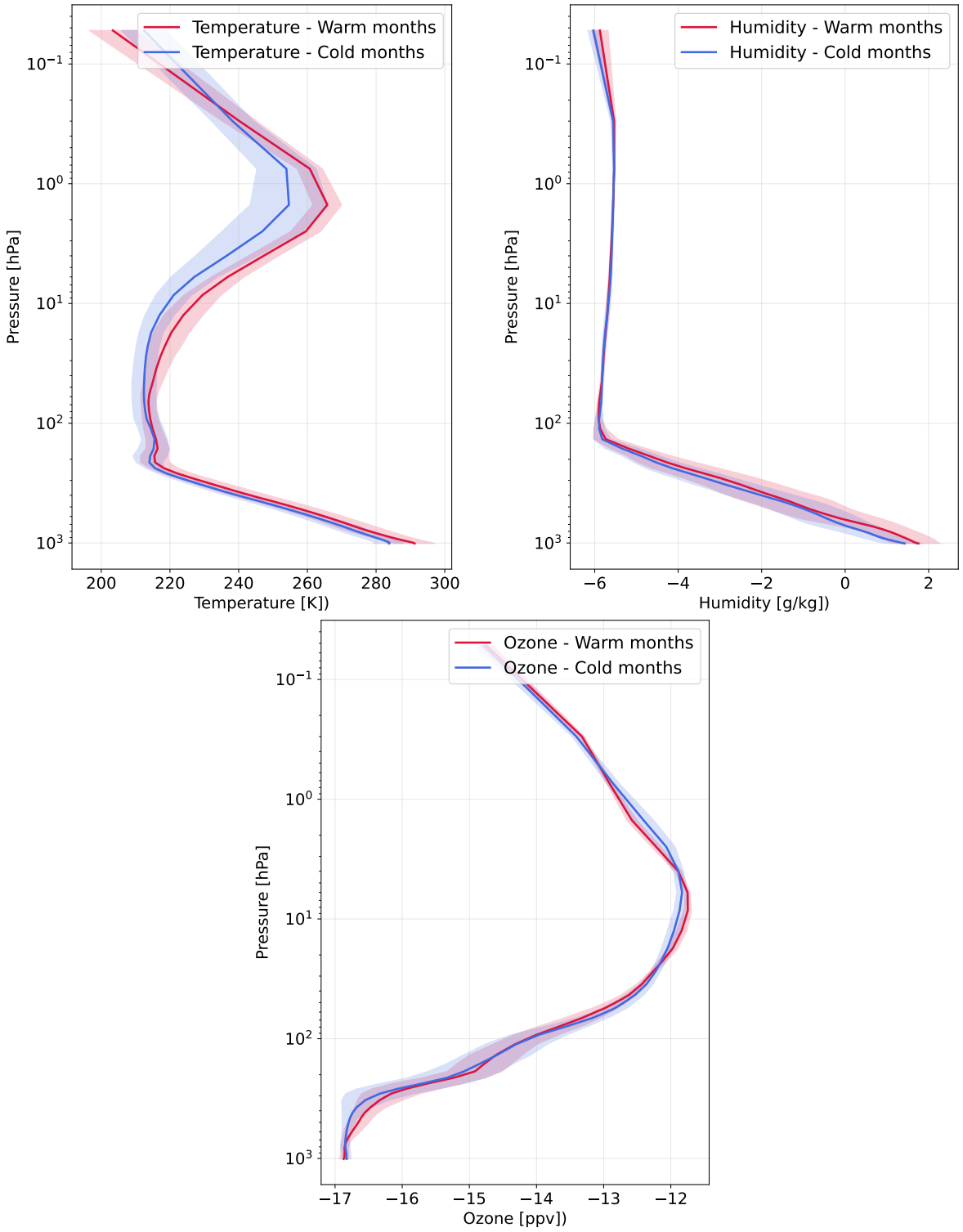

Figure 3.7: *Prior temperature, humidity and ozone profiles for warm (red line) and cold months (blue line) on the σ pressure grid. The shaded areas are the relative standard deviation. Humidity and ozone are in the logarithmic scale, the same used in the inversion model*

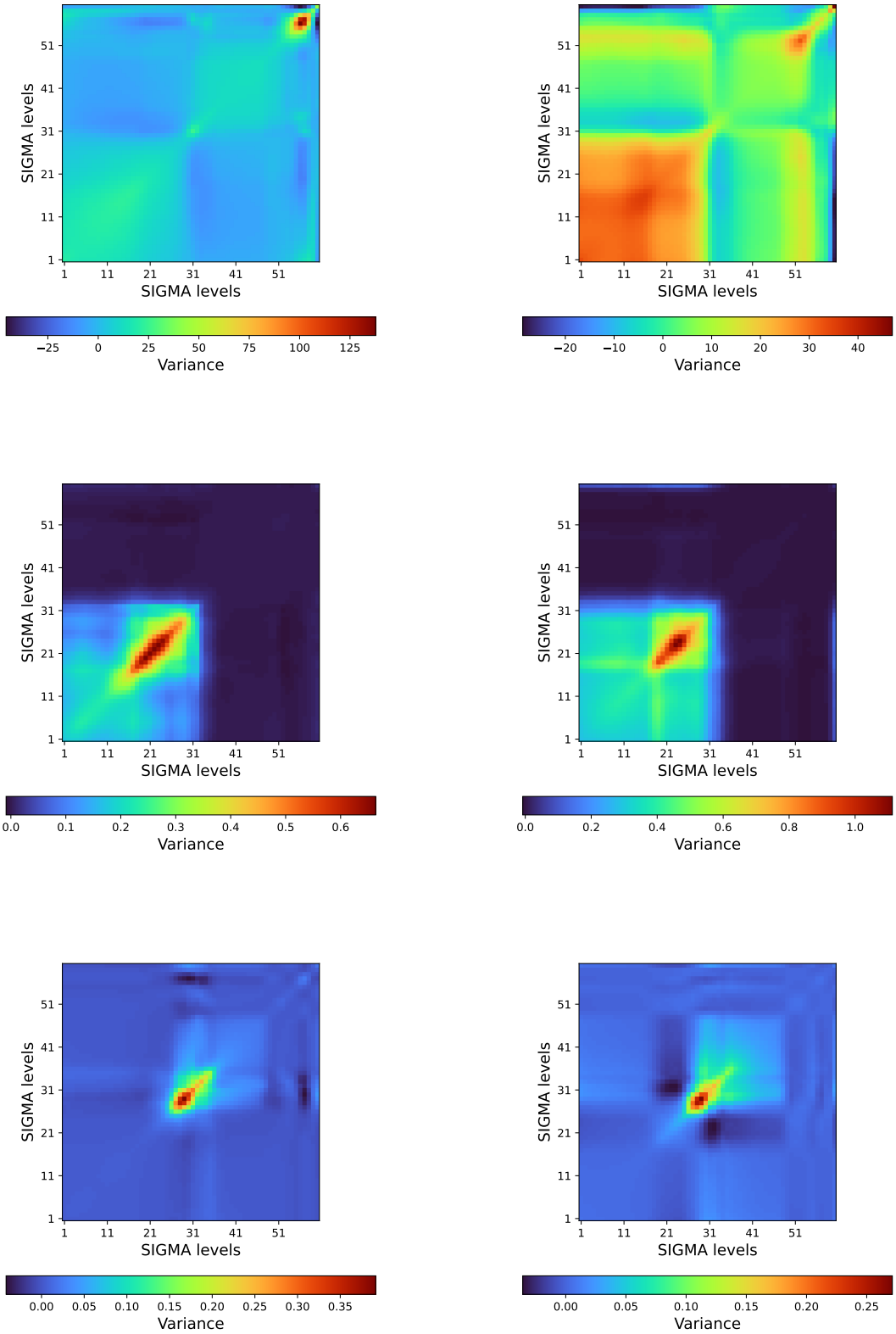

Figure 3.8: *Temperature (upper panels), humidity (middle panels) and ozone (lower panels) covariance matrices for warm and cold months on the σ levels. Humidity and ozone matrices are in a logarithmic scale*

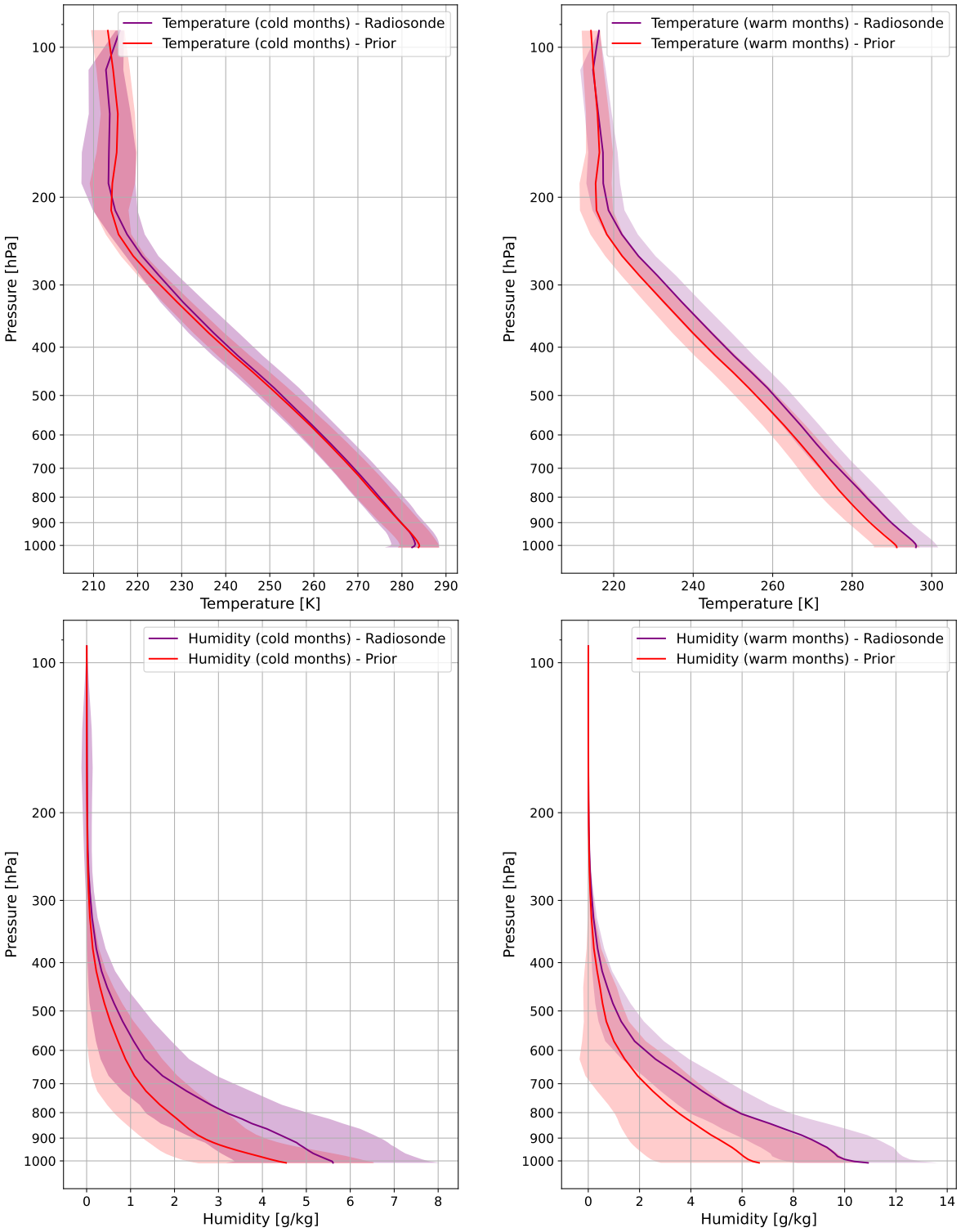

Figure 3.9: *Comparison of temperature and humidity profiles for warm and cold months on the σ levels between the prior (ERA5) and the mean of the radiosonde. The two shaded areas are the standard deviations of the two datasets. Profiles are interpolated on the σ pressure levels and shown up to 100 hPa*

concentrations in the atmosphere, as well as on carbon fluxes between the atmosphere, the earth and oceans. It provides daily data on molar fraction of atmospheric CO_2 and CH_4 at 8.0 m from the surface; we computed the monthly mean of these values and used it to correct the input climatological profiles of the algorithm.

Aerosol

The level of non-linearity of the model increases significantly once aerosols are introduced into the retrieval framework. In contrast to the clear-sky case, the presence of this type of particles requires the treatment of multiple scattering processes, which are taken into account through the Chou approximation, allowing us to simplify the forward model that would be otherwise be extremely complex under these conditions. Furthermore, the introduction of an aerosol layer represents a marked structural discontinuity relative to the clear-sky configuration. The inverse problem, which is already intrinsically ill-posed, therefore becomes even more unstable when aerosol parameters are included in the state vector. For this reason, the adoption of an appropriate regularization strategy remains essential; in particular, the choice of a suitable a prior covariance matrix plays a crucial role in stabilizing the inversion.

We now describe how the covariance matrices for the aerosol have been constructed. The original covariance matrices were developed for ice clouds; however, they can be consistently applied to aerosol as well. While the absolute values of particle radius and dust content are adapted to reflect typical aerosol properties, the underlying covariance formulation primarily describes the spatial correlation of the variables rather than their specific microphysical nature. From this perspective, it is reasonable to assume that the geometric structure of an aerosol layer is comparable to that of an ice cloud layer. Therefore, the same correlation scales and structural assumption used for ice clouds can be adopted for aerosols and the same covariance matrix will be used.

To build the ad-hoc covariance matrix we assume a Gaussian-like shape for the vertical structure of clouds. We extracted the ice mass content profiles from the SAF database of the Numerical Weather Prediction [34] which is then interpolated onto the σ pressure grid. For each layer, an average value of ice water content was computed. The effective dimension of the ice clouds particles is computed using the average value of ice content, temperature, pressure and water vapor mixing ratio (also taken from SAF database) [47]. A state vector combining both ice mass content and effective particle size is then constructed, allowing to retain the relationship between cloud particle effective size and ice content. From this state vector we can compute mean and covariance matrix. To simplify the prior description, only clouds with a single-mode vertical profile of ice content are used to generate the statistics. Among these profiles,

only those exceeding 0.25 g/kg at any level are retained for the covariance matrix. The same logarithmic transformation used for water vapor mixing ratio is applied. A Gaussian kernel is convolved over the covariance matrices, obtaining a smoother prior and introducing Gaussian correlations between physical quantities across different model levels. Furthermore, a tapering procedure is applied to the covariance matrix in order to suppress non-physical correlations between model levels.

For the mean state, aerosol statistics from the SAF dataset are computed. In particular, we selected desert dust aerosol and extracted the typical radii and dust content.

Once the prior state is defined, additional transformations can be applied to generate different realizations of aerosol properties. In particular, the vertical position of the prior profile can be shifted within the model grid. This operation allows the prior statistics to better represent dust structures occurring at different altitudes.

In this work, two covariance matrices for radius and content were used (shown in Fig.3.10), relative to a low and a very low aerosol layer.

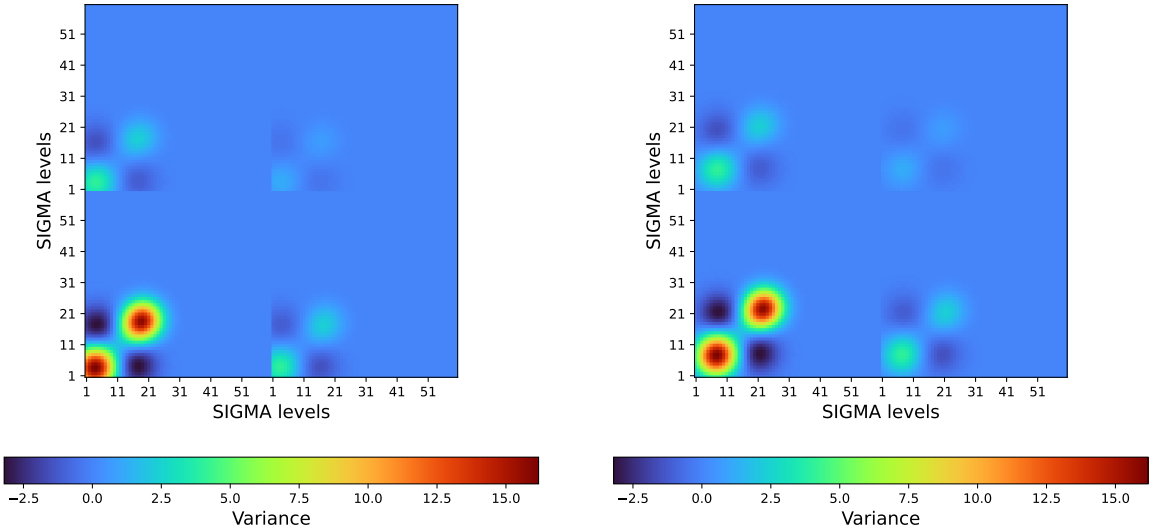

Figure 3.10: *Dust covariance matrices. In the left panel the very low level one, in the right panel the low level one*

Chapter 4

Results and discussion

4.1 Preliminary optimizations

After setting all the physical parameters of the state vector, it is possible to proceed with the analysis and tuning of some of the inversion parameters. In particular, the inflation parameter γ of the covariance matrix (Eq.2.29), the emissivity correlation length and its covariance matrix were tuned. The objective of the tuning is to identify the parameter values that optimize the solution. This step is particularly necessary because of the ill-posedness of the inversion problem. In such problems, the solution is non-unique, unstable, and highly sensitive to modeling errors. The tuning of hyperparameters, such as the covariance inflation factor and the correlation length, play a regularizing role: it controls the balance between prior information and observations, stabilizes the solution and mitigates the amplification of noise. Therefore, an appropriate tuning is essential to obtain a physically consistent, robust, and reliable solution.

For all the parameters, the χ^2 criterion was adopted as the optimization method. Specifically, the parameters were systematically varied, and the values corresponding to the minimum χ^2 were selected. The spectral range selected is : [650 - 1250] cm^{-1}, the same one that will be used for the aerosol analysis. A subset of 12 elements, 1 for each month, is selected for the optimization.

Inflation factor γ

The inflation parameter controls the balance of information between the prior and the observations: the larger its initial value, the greater the weight assigned to the prior. During the iterative process, this parameter is progressively reduced until it reaches 1. However, the choice of the initial value requires careful investigation, as it can significantly influence the convergence behavior and the stability of the solution.

We tested three initial values: 1000, 300 and 100 and we compared the χ^2 of the inversions in 12 cases.

The results of the optimization are shown in Tab.4.1 from which we can conclude that 1000 is the best initial inflation factor, which is the same value used in [32].

γ **value**	**mean** χ^2
1000	1.2732
300	1.2978
100	1.3226

Table 4.1: *Summary table reporting, for each inflation factor* γ *used, the mean* χ^2 *obtained for the 12 studied cases*

Emissivity correlation length

The correlation length (CL) is a measure of the order in a system and describes how variables, in our case emissivity, at different positions (wavenumbers) fluctuate together on average. In other words, it defines the typical distance beyond which two points can be considered nearly independent.

Optimizing the correlation length is important because it directly influences the balance between resolving fine scale structures and preventing noise amplification. If the correlation length is too small, the inversion may fit high wavenumber noise, leading to unstable or physically unrealistic solutions. Conversely, if it is too large, the solution may be overly smooth and fail to capture meaningful variability. Therefore, tuning this parameter allows one to identify the spatial scale that best represents the physical variability of emissivity while ensuring stability and consistency of the retrieved solution.

We tested 5 different values: 5, 15, 50, 200 and 500. Since the prior emissivity vector is defined on a spectral grid with a resolution of 1 cm^{-1}, these values correspond to correlations spanning 5, 15, 50, 200, and 500 spectral points, respectively.

Results are shown in Tab.4.2, indicating that the best choice for CL value is 200.

CL value	**Mean χ^2**
5	0.908
15	0.891
50	0.894
200	0.883
500	0.889

Table 4.2: *Summary table reporting, for each correlation length for used, the mean χ^2 obtained for the 12 studied cases*

Emissivity variance

As discussed in Sec.3.4, and recalling the considerations on the role of prior covariance matrices in ill-posed problems, the choice of the prior statistics is crucial for the stability and quality of the retrieval. While the mean prior state of emissivity was derived from the statistics of the Huang dataset, the corresponding variance proved not to be suitable for our application. In particular, the covariance computed in this way was found to be very small, due to the limited variability present in the dataset. For this reason, instead of adopting the natural physical variability, a prior variance defined by a vector of ones was chosen. This choice was motivated by the comparison of the results of inversions (performed on the same cases considered in the two previous optimization steps) and evaluating the two alternative variance assumptions. The emissivity values retrieved using the two different variances are statistically compatible with each other. However, when using the variance computed from the Huang dataset, 3 out of 12 inversions don't converge and for the convergent cases the χ^2 values are higher than those obtained with the alternative variance. In contrast, when using the unit variance vector, all retrievals converge successfully and exhibit lower χ^2 values. Therefore, given the statistical compatibility of the results and the improved χ^2 performance, the unit variance formulation was adopted for emissivity covariance.

4.2 Clear-sky retrievals

After conducting a preliminary optimization study on selected inversion settings, we are now ready to perform the first retrievals under clear-sky conditions. In this section, we will present the results obtained from these retrievals and provide a thorough analysis. The retrieved quantities will be compared with independent measurements from radiosondes, allowing us to assess the accuracy and reliability of the inversion approach. After this comparison, an analysis of the averaging kernel and on the radiance

residuals are made. Finally, an initial assessment of the aerosol impact is carried out by dividing the dataset into aerosol-affected and aerosol-free cases and investigating potential differences in the clear-sky retrieval results.

After the cloud selection, a total number of 362 inversions is performed, according to the convergence criteria described in Sec.2.2 8 of them (all in warm months) didn't reach convergence and where excluded from the statistics.

Comparison with radiosonde measurements

In this paragraph, we present the comparison between the retrieved atmospheric profiles of temperature and humidity and independent radiosonde measurements. This type of validation provides a straightforward and intuitive way to asses the quality of the retrieval, as radiosonde measurements are considered a reliable reference for vertical atmospheric structures. However, this comparison is not entirely trivial and requires careful consideration due to the completely different nature of the two measurements. The two instruments differ in sampling characteristics, vertical resolution, spatial representativeness, and measurement principles. In addition, other practical factors must be considered. First, the temporal availability of radiosonde data does not fully overlap with the retrieval dataset; therefore, the comparison is necessarily restricted to cases in which in situ measurements are available. Second, we must consider that the spatial distance between the satellite pixel and the radiosonde launch site can be up to 12 km and that there is a temporal mismatch between the observations. To mitigate the impact of the temporal mismatch, a time interpolation is performed prior to the comparison. In particular, the radiosonde profiles closest in time are linearly interpolated, with weights determined by their temporal distance from the corresponding IASI observation. This procedure aims to provide a more representative profile at the satellite overpass time, thereby reducing artificial discrepancies due to timing differences rather than to retrieval performance.

To account for the intrinsic smoothing of the retrieval and to reduce the difference in the vertical resolution of the retrieval and the radiosonde measurement, the comparison is further performed by explicitly considering the averaging kernel matrix. Starting from Eq.2.20 and neglecting the spectral error terms ($\boldsymbol{G\epsilon}$), the equation can be rearranged as:

$$\hat{\boldsymbol{x}} = \boldsymbol{x}_a + \boldsymbol{A}(\boldsymbol{x} - \boldsymbol{x}_a) \tag{4.1}$$

that shows how the retrieved state is not the "true" state $\boldsymbol{x}$, but rather a smoothed version of it, where the smoothing is governed by the averaging kernel matrix $\boldsymbol{A}$. In our case, we can substitute $\boldsymbol{x}$ (as it is not known) with the measurement of the radiosonde. Therefore, to obtain the radiosonde profile consistent with the vertical sensitivity of

the retrieval, we compute:

$$\boldsymbol{x}_c = \boldsymbol{x}_a + \boldsymbol{A}(\boldsymbol{x}_{radiosonde} - \boldsymbol{x}_a) \tag{4.2}$$

where $\boldsymbol{x}_c$ represents the profile weighted with the averaging kernel. In practice, with this operation we ensure that the comparison is performed at the real vertical resolution of the retrieval.

To do the actual comparison between the two quantities we compute the residual $\boldsymbol{x}_{rs}$ between the retrieved temperature and humidity profiles $\boldsymbol{x}_{opt}$ and the in situ measurement, defined as the difference between the two quantities:

$$\boldsymbol{x}_{rs} = \boldsymbol{x}_{opt} - \boldsymbol{x}_c \tag{4.3}$$

The residuals are shown in Fig.4.1, where the individual residual profiles are shown together with the mean residual profile, which provides an estimate of the systematic bias of the retrieval. In addition, the red (blue) shaded area represents the root mean square error (RMSE) computed between the retrieved profiles and the convolved radiosonde profiles for temperature (humidity), thus quantifying the overall retrieval error at each level. The second orange (light blue) shaded band indicates the standard deviation of the radiosonde measurements of temperature (humidity), providing a measure of the natural atmospheric variability. The results are shown from the surface up to 100 hPa, corresponding to the maximum altitude for which in situ measurements are available. The comparison is based on 250 retrieval-radiosonde pairs.

The temperature residuals exhibit a mean negative bias of approximately 1 K in the lowest atmospheric layers, indicating that the retrieval underestimates temperature close to the surface. A second negative bias is observed in the upper part of the analyzed domain, increasing in magnitude toward 100 hPa. Outside these two regions, the mean bias generally remains within $\pm$ 0.5 K, suggesting a good overall agreement between the retrieved and radiosonde profiles throughout most of the troposphere.

Regarding the error magnitude, the RMSE remains smaller than the standard deviation of the radiosonde measurements at almost all pressure levels, with the exception of the region near 100 hPa. This behavior indicates that the retrieval error does not dominate over the intrinsic variability of the atmospheric state.

Humidity residuals show a behavior partially analogous to that observed for temperature. In the lowest atmospheric layers, a negative mean bias of slightly less than 1 g/kg is evident, indicating that the retrieval tends to underestimate moisture near the surface. As for temperature, this feature may be related to the greater complexity of retrievals within the boundary layer, where strong vertical gradients and pronounced spatial variability can challenge the inversion. Above the lower troposphere, the mean

bias rapidly approaches zero. At these levels, both the retrieved and measured humidity values are typically very small, often close to zero, which naturally limits the magnitude of the residuals. Consequently, the radiosonde standard deviation and the RMSE are also nearly zero. In the lower troposphere, where moisture content and variability are largest, the RMSE remains systematically smaller than the radiosonde standard deviation.

Both negative biases for temperature and humidity near the surface are consistent with the bias observed between the prior and the radiosonde profiles, as already shown in the Fig.3.9.

Overall, temperature and humidity retrievals demonstrate good accuracy throughout most of the troposphere, with systematic deviations confined near the surface and upper level regions.

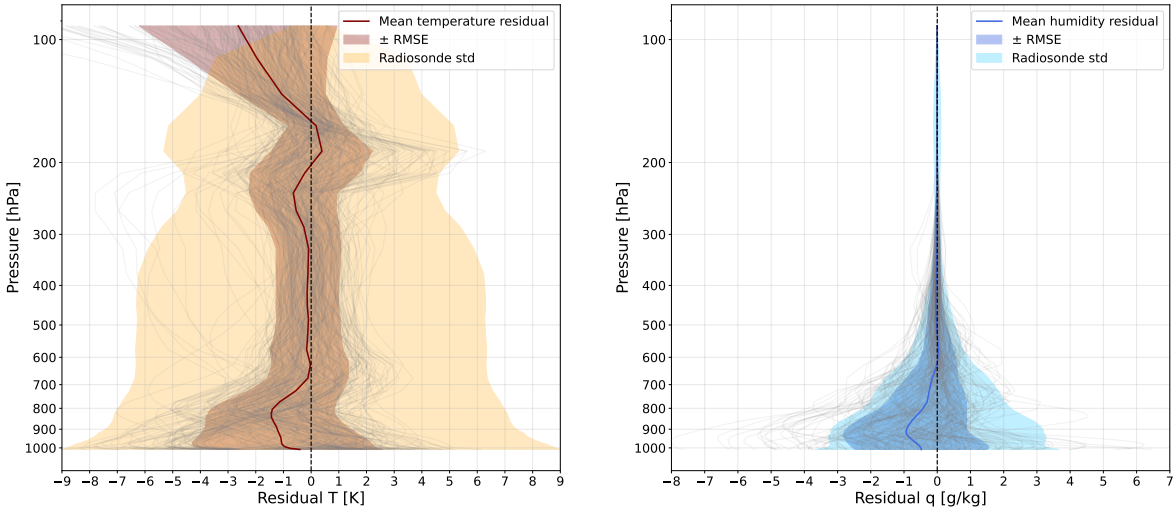

Figure 4.1: *Residuals between retrieved temperature (left) and humidity (right) profiles and the radiosonde measurements. Grey lines are the single residuals, the red line is the mean residual for temperature, blue line is the mean residual for humidity. The orange (light blue) shaded area is the standard deviation of the temperature (humidity) radiosonde profiles and the shaded red (blue) area is the RMSE between retrieved and radiosonde profiles.*

Comparison with Level 2 IASI

In order to provide a more comprehensive evaluation of the retrieval performance, we also analyze the residuals between the IASI Level 2 products and the radiosonde measurements.

Before comparing these two products it is necessary to check the *flag_retcheck* parameter, which indicates whether the retrieval was successful. All products for which

this flag is equal to 1 are therefore excluded from the analysis. After this quality control step, 238 valid cases remain, i.e., 12 fewer than in our retrieval dataset. The comparison is carried out using both the radiosonde profiles and the Level 2 profiles interpolated onto the σ pressure grid, in order to ensure consistency with the methodology adopted in the previous analysis. However, it is important to emphasize that in this case the radiosonde profiles are not convolved with the averaging kernel, since this information is not available in the L2 data products. Residuals are shown in Fig.4.2. As observed, for both variables the mean bias and the mean error are smaller than those obtained with our retrieval (Fig.4.1). In addition, the mean bias profile appears less smooth; this behavior is primarily due to the absence of the convolution of the radiosonde profiles with the averaging kernel, which tends to smooth the vertical structures and reduce small scale variability in the residuals.

It is import to highlight a major difference between our retrieval and the one used to generate the Level 2 products, namely the initial guess. While our inversion is initialized using a six-months climatological profile, the IASI L2 products use as first guess a profiled derived from a statistical retrieval (3.2.2). This difference can significantly affect the quality of the retrieval and its convergence properties. Therefore, it is entirely reasonable that L2 retrieval exhibits a better overall performance. Nevertheless, it remains noteworthy that the bias obtained with our retrieval is still low, confirming the robustness and reliability of our approach.

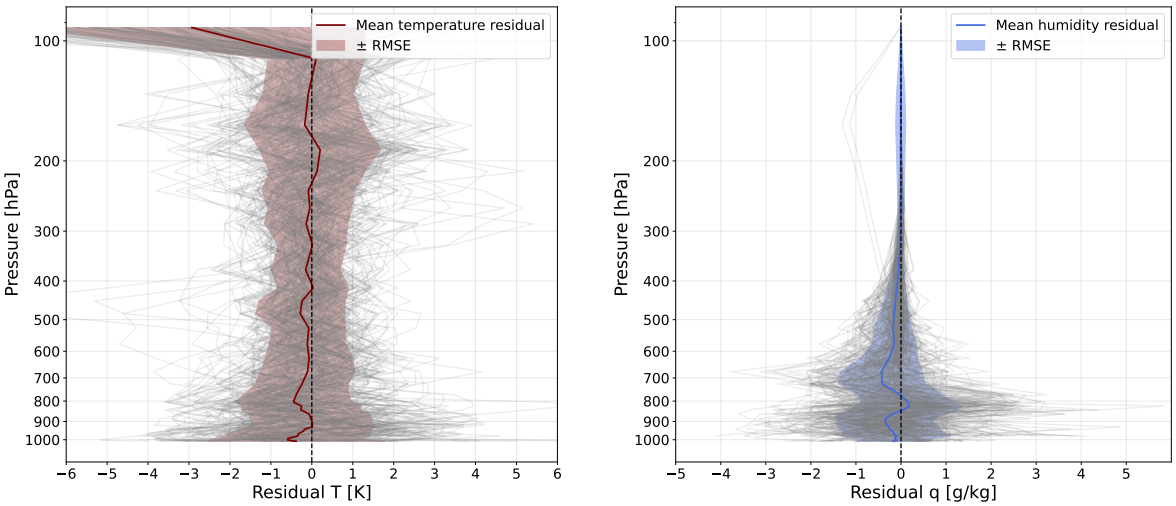

Figure 4.2: *Residuals between IASI Level 2 temperature (left) and humidity (right) profiles and the radiosonde. Grey lines are the single residuals, the red (blue) line is the mean residual for temperature (humidity), shaded red (blue) area is the RMSE between retrieved and radiosonde profiles*

Averaging kernel and information content

In order to better interpret the performance of the retrieval, it is essential to analyze the averaging kernel associated with the variables. The averaging kernel matrix provides a quantitative measure of the vertical sensitivity of the inversion, indicating from which atmospheric layers the retrieved information effectively originates. Presenting the averaging kernel is therefore particularly meaningful when discussing the residuals with respect to the radiosonde observation: by comparing the vertical structure of the residuals with the sensitivity indicated by the averaging kernel, it is possible to identify the levels where the retrieval is truly driven by the measurements and those where larger discrepancies might be related to limited vertical resolution and stronger prior dependence. The diagonals of the averaging kernel matrices for temperature and humidity up to 100 hPa are shown in Fig.4.3. Both plots show that the sensitivity near the surface is lower than in the mid-troposphere, indicating that in the lowest layers the retrieval is more strongly influenced by the *a priori* information. In contrast, the mid-troposphere exhibits higher averaging kernel values, meaning that a larger fraction of the retrieved information originates directly from the measurements. This behavior may help explain the origin of the negative bias observed near the surface. Since the retrieval in these layers is more prior-driven, any bias already present in the prior with respect to the radiosonde profiles is likely to propagate into the final retrieval. Therefore, the reduced measurement sensitivity close to the surface, combined with the existing prior bias relative to the radiosondes, provides a consistent interpretation of the observed negative bias.

Spectral residuals and χ^2

In this section, we focus on the retrieval results in terms of the spectra residuals between the observed and retrieved radiances and the χ^2 statistics. These diagnostics provide a quantitative assessment of the consistency of the solution and of the agreement between observations and forward model simulations.

In particular, we focus on the comparison between the residuals and the χ^2 distribution of the first step of the retrieval (i.e. the ones computed from the prior) and the ones computed from the optimal state at the end of the retrieval. This analysis allows us to understand the capability of the retrieval to reduce systematic discrepancies between measured and simulated radiances from the first guess. We can quantify the improvement achieved by the inversion and verify if the remaining differences are consistent with instrumental noise and model errors.

Initial and final mean residuals are shown in Fig.4.4 and Fig.4.5. The mean initial

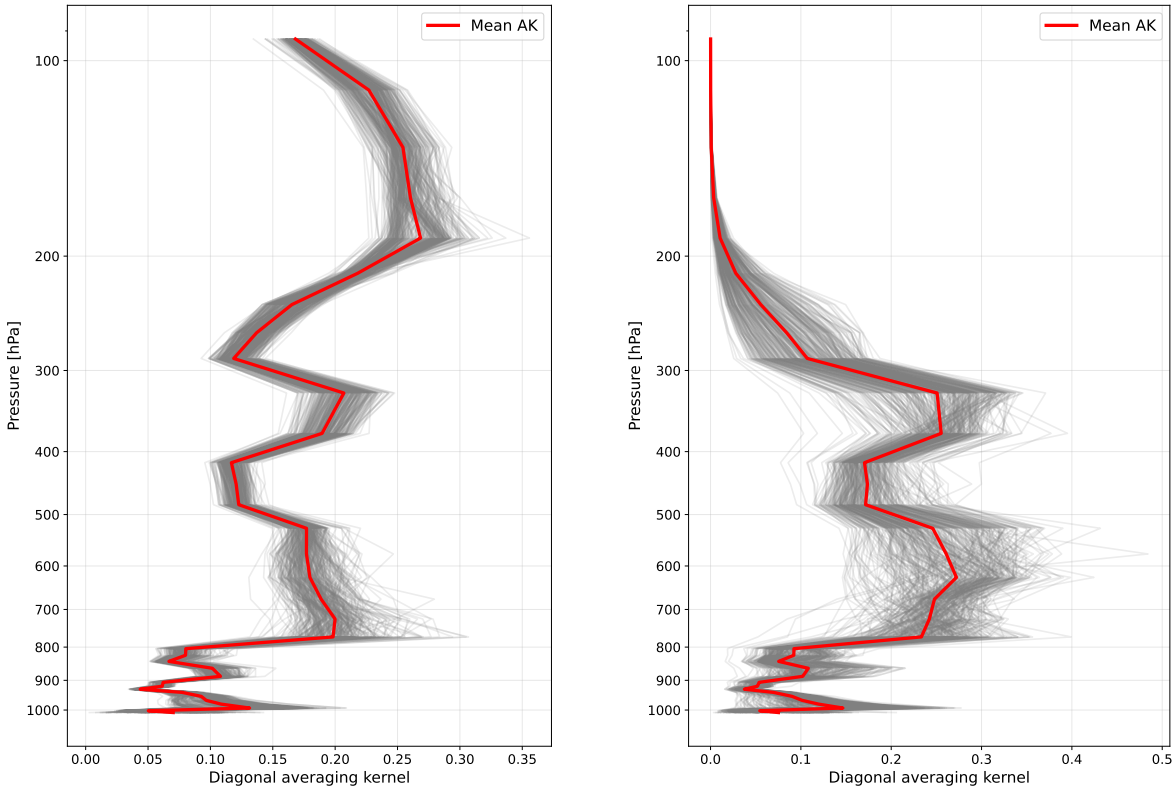

Figure 4.3: *Diagonals of the averaging kernel matrices of the retrieved temperature (left panel) and humidity (right panel). In gray lines all the diagonals of the averaging kernels and the red line is the mean diagonal averaging kernel*

spectral residuals clearly show that the radiances simulated from the first guess (i.e., the prior state) are significantly different from the observed ones: the first guess alone is not sufficient to reproduce the measured radiances and leaves systematic discrepancies across all the spectral regions. The large amplitude of these residuals indicate that the a priori atmospheric state is far from the true state of the atmosphere, providing an initial indication of the need for a substantial correction by the inversion. In contrast, the mean final residuals, computed using the radiances simulated from the optimal state, are strongly reduced in magnitude. They fall almost entirely within the expected instrumental noise level of IASI and no longer exhibit clear spectral structures. The residual spectrum appears largely unstructured and resembles white noise, with only a few isolated spikes exceeding the noise level. This behavior indicates that the retrieval has successfully captured the relevant atmospheric information contained in the measurements. The few spikes that exceed the noise level may plausibly be associated with limitations in the forward model. In particular, they could arise from incomplete or imperfect spectroscopic representation, for example due to trace gases that are not included in the state vector or are entirely neglected in the forward calculation.

A fully consistent picture emerges from the analysis of the χ^2 statistics, shown in Fig.4.6 and Fig.4.7. The initial χ^2 values, computed using radiances simulated from the first guess state, are generally very large, reflecting the substantial mismatch already highlighted by the spectral residuals. On the other hand, the final χ^2 values, computed at convergence using the optimal state, are significantly reduced. Two cases were removed from this distribution as they had a high (greater than 1.2) χ^2 of convergence. This distribution exhibits the typical behavior for a well-convergent retrieval. It is import to stress that the χ^2 shown in these two distributions is not the standard definition based solely on observation-space residuals. Instead, it corresponds to the generalized form described in Eq.2.32, that combines the contribution from the residual in the observation space with the deviation of the state state vector from the a priori, weighted by their respective covariance matrices. In addition, the covariance matrix of the IASI measurements is inflated by a factor 2. For this reason, the expected value is not 1.

We also show in Fig.4.8 the χ^2 distribution computed using the standard formula:

$$\chi^2 = \frac{(\boldsymbol{y}_{opt} - \boldsymbol{y}_m)^T \boldsymbol{S}_\epsilon^{-1} (\boldsymbol{y}_{opt} - \boldsymbol{y}_m)}{len(y_m) - n_{PC}}$$

where $\boldsymbol{y}_m$ is the measured radiance, $\boldsymbol{y}_{opt}$ is the radiance of the optimal state and n_{PC} is the total number of principal components used in the problem (92). In this case, the mean value of χ^2 is 1.01 and the maximum of the distribution is located at $\chi^2 = 0.904$.

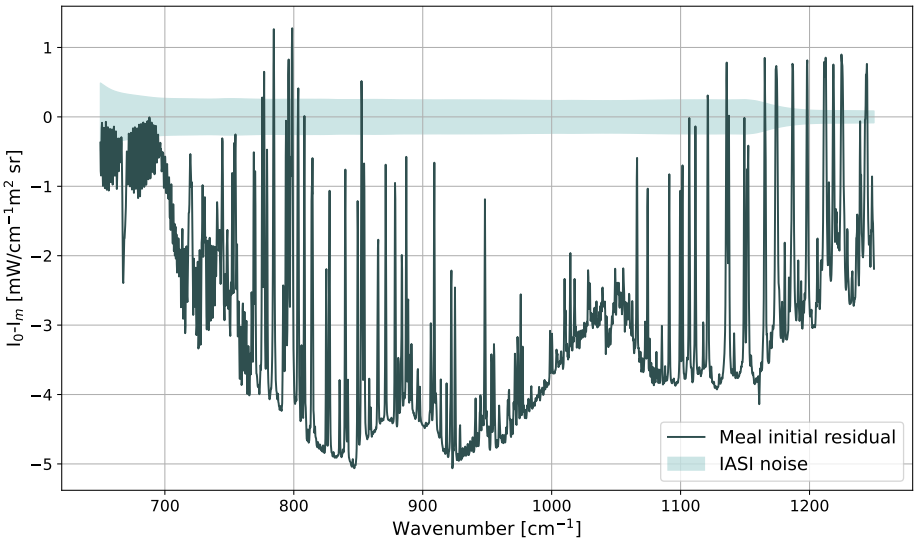

Figure 4.4: *Mean residual between the radiance computed from the first guess and the measured radiance. The shaded green area corresponds to the error in the measurements*

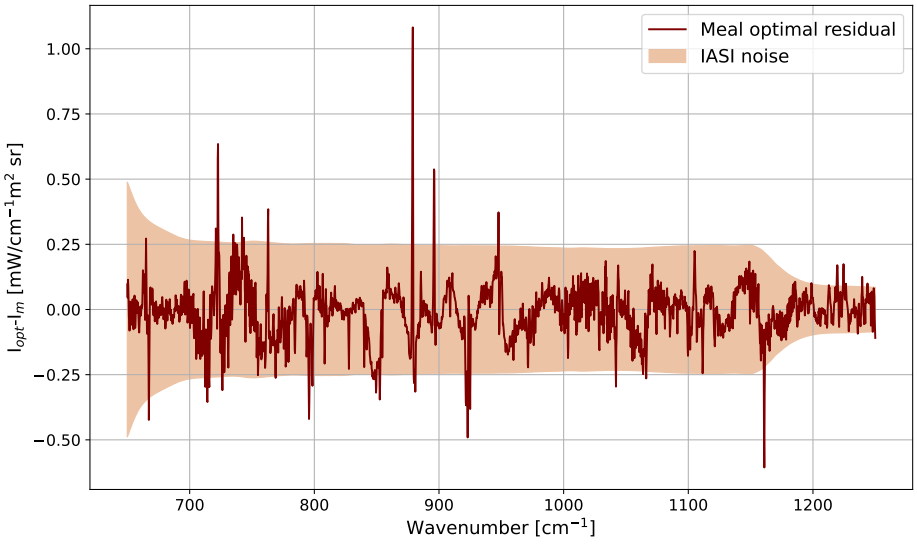

Figure 4.5: *Mean residual between the radiance relative to the optimal state and the measured radiance. The shaded orange area corresponds to the error in the measurements*

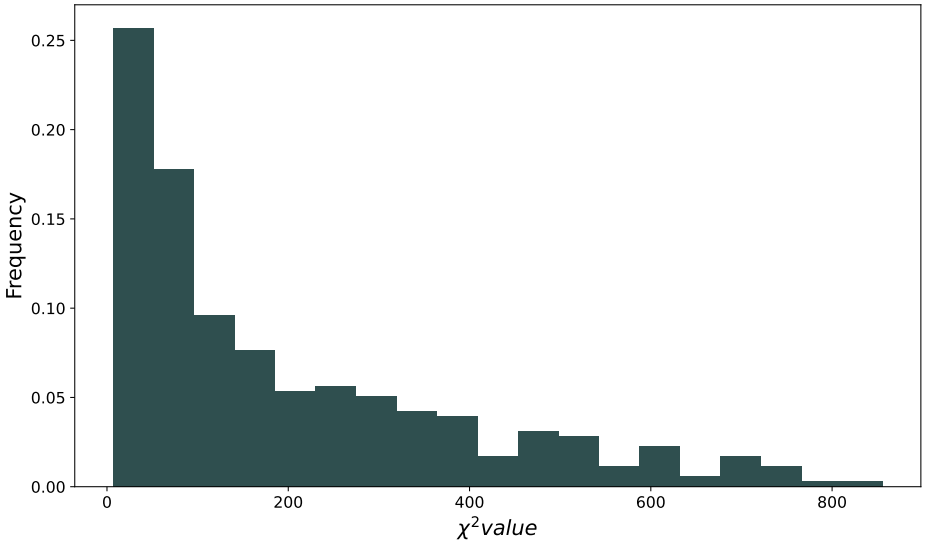

Figure 4.6: *Initial (prior) χ^2 distribution*

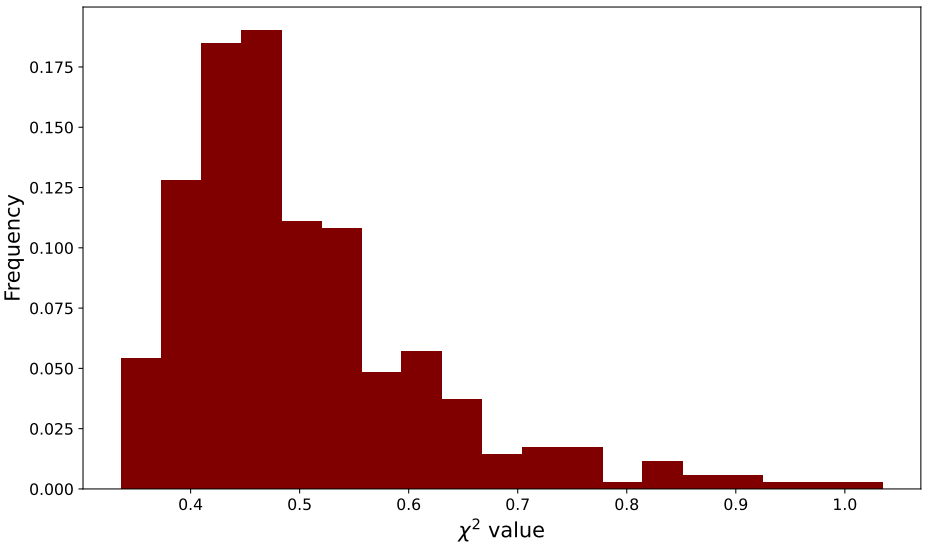

Figure 4.7: *Final (optimal) generalized χ^2 distribution*

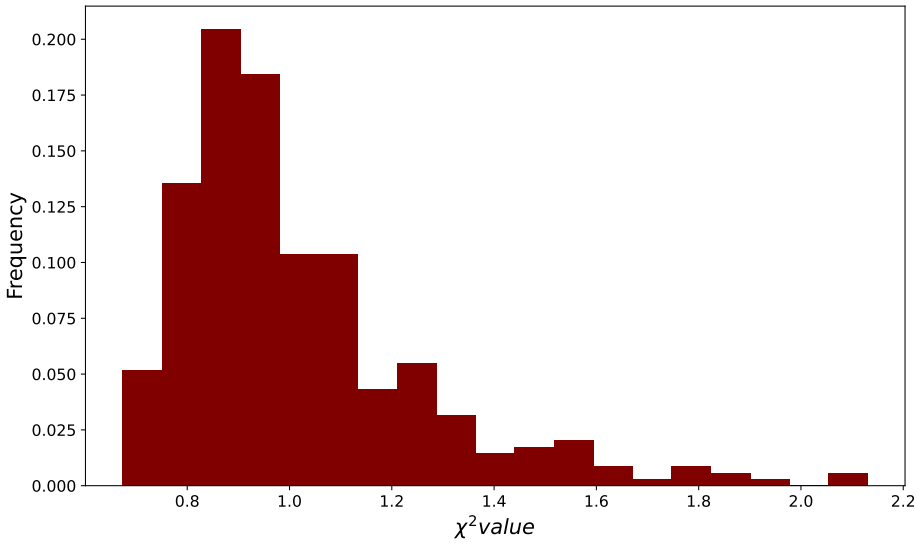

Figure 4.8: *Final (optimal) χ^2 distribution computed with the standard formula*

Other analysis

In order to further investigate the performance of the retrieval algorithm, we now analyze how the retrieval quality varies with geometry of the measurement. One important geometric parameter is the satellite zenith angle, which describes the angle between the sensor's line of sight and the local vertical at the target. This angle directly affects the optical path length through the atmosphere, altering the amount of radiation entering the satellite. As a consequence, retrieval errors can exhibit a dependence on viewing angle, especially at larger zenith angles where the actual path through the atmosphere is longest.

In this context, plotting the χ^2 values against the satellite zenith angle provides a qualitative way to evaluate how consistently the forward model matches the measured radiances under different viewing geometries. In Fig.4.9 we show a scatter plot between the χ^2 (computed with the generalized formula from Eq.2.32) and the satellite zenith angle values. The scatterplot reveals a slight increase in χ^2 values with increasing satellite zenith angle, particularly for larger angles approaching 60°. This trend suggests a modest degradation in retrieval performance as the viewing angle increases. Such behavior is physically consistent with the longer atmospheric optical path. However, the degradation is not severe, as the observed increase remains limited in magnitude. The retrieval algorithm therefore appears to maintain overall stability across all the angular range, with only moderate loss of fit quality at high zenith angles.

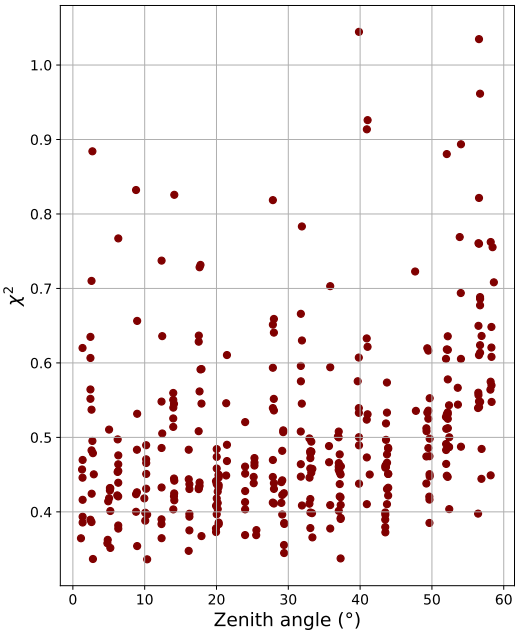

Figure 4.9: *Scatterplot of χ^2 values (computed with the generalized formula) and measurement zenith angles*

Looking for dust signals in clear-sky retrievals

The retrievals were performed on cases that had been classified as clear-sky, according to the IASI Level 2 classification. However, in addition to the cloud flag, the Level 2 data also provide the specific dust index flag indicating the presence of aerosol. A significant number of cases labeled as clear-sky exhibit a positive dust flag. In this section, we investigate this aspect by dividing the clear-sky dataset into two subsets: cases flagged with aerosol and cases without it. The presence of dust is suspected when the index is greater than approximately 2 [7]. The objective is to assess whether systematic differences emerge in the inversion results between these two subsets. Since the retrievals were carried out under a clear-sky configuration (assuming a cloud fraction equal to zero), any discrepancies observed between the two groups may be attributable to the unaccounted presence of aerosol and its radiative impact. This analysis therefore aims to evaluate the potential impact of aerosol contamination on the inversion performance under clear-sky assumptions.

The analysis was first carried by a visual inspection of the radiance and the brightness temperature and then by examining in a more quantitative way wether retrieval residuals and biases correlate with scenes flagged for dust presence.

The first analysis was performed by comparing the radiances and brightness temper-

atures from IASI observations, dividing the cases according to the presence or absence of dust, as indicated by the flag. In addition, data were further subdivided by day and hour in order to reduce the variability associated with changes in atmospheric temperature and humidity. This temporal classification allows us to minimize the impact of thermodynamic variability and to better isolate potential differences attributable solely to the radiative effect of aerosol.

However, this analysis did not yield clear or systematic results: no distinctive or recurrent spectral features could be identified in the IASI measurements in association with cases affected by aerosol. This outcome is likely due to the fact that, despite the careful temporal classification, the variability in the other atmospheric variables has a much stronger influence on the observed spectra than the radiative effect of dust and the aerosol signal may be masked. Overall, this preliminary analysis confirms that, within the spectral range considered in this study, the radiative contribution of aerosol is relatively small compared to other atmospheric factors.

We therefore proceed to analyze the results of the retrievals, focusing in particular on the residuals with respect to the radiosonde measurements and on the distribution of the χ^2 values. The dataset is again classified according to the presence (102 cases) or absence (245 cases) of a positive dust flag (i.e. dust index bigger than 2). In Fig.4.10 the residuals between temperature and water vapor mixing ratio retrieved and measured by the radiosonde for cases with no aerosol are shown. In Fig.4.11 the residuals of the cases classified as dusty are shown. The figures indicate that, for both temperature and humidity retrievals, the negative bias observed near the surface is reduced in the cases without aerosol. In contrast, scenes affected by aerosol tend to exhibit a more pronounced negative bias in the lowest atmospheric layers. This behavior may be interpreted as an indication that the absence of the aerosol inclusion in the inversion scheme, when aerosol is actually present in the scene, forces the retrieval algorithm to compensate through adjustments in other atmospheric variables. The inversion may modify temperature and humidity profiles to account for the radiative effects that are in reality due to aerosol.

We now evaluate the goodness of the retrieval by comparing the χ^2 distributions (computed with the standard formula) for aerosol and no aerosol scenes. The result is shown in Fig.4.12. The figure shows a clear difference between the two distributions. In aerosol conditions, the χ^2 distribution is shifted towards higher values, with peak occurring at larger χ^2 and the presence of some cases characterized by very high χ^2 values. In contrast, the distribution for clear-sky scenes is shifted toward lower values, with a peak at smaller values and generally more confined spread.

This behavior indicates that the residuals between the observed and simulated

radiances are worse when aerosol is present. The better performance in no aerosol cases confirms the internal consistency of the retrieval under conditions that are more consistent with the model assumptions (i.e. a clear sky scenario).

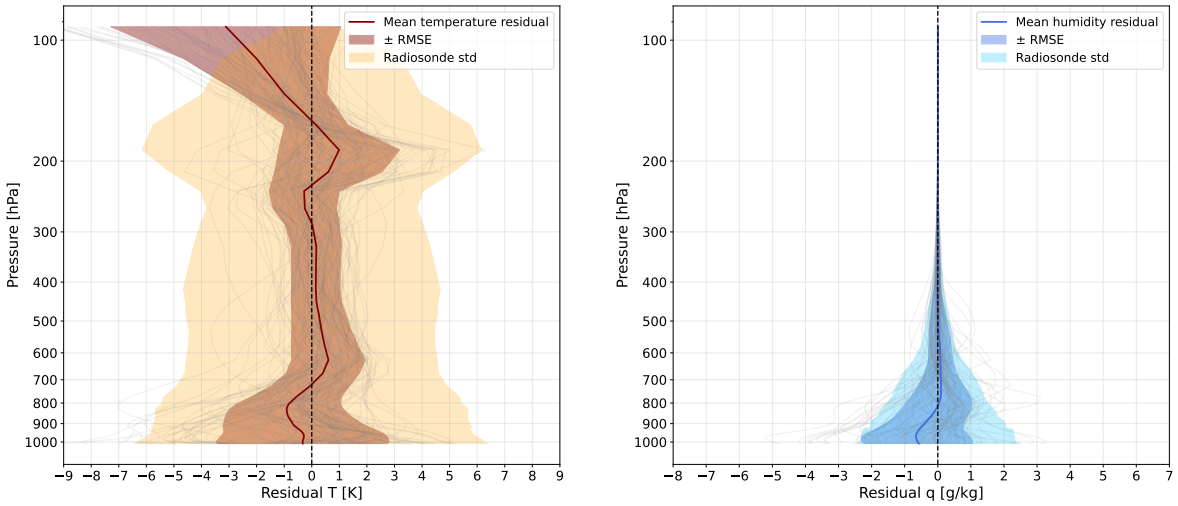

Figure 4.10: *Residuals between retrieved temperature (left) and humidity (right) profiles and the radiosonde considering only cases classified (according to the dust flag) as without aerosol. Grey lines are the single residuals, the red line is the mean residual for temperature, blue line is the mean residual for humidity. The orange (light blue) shaded area is the standard deviation of the temperature (humidity) radiosonde profiles and the shaded red (blue) area is the RMSE between retrieved and radiosonde profiles. All the retrieval are performed considering clear-sky scenes*

4.3 Aerosol retrievals

After performing the inversions using the clear-sky configuration of the retrieval, we now present results for a subset of cases that, although classified as clear sky, exhibit the presence of aerosol according to the dust flag indicator. In this study, we focus on transported dust.

Before proceeding with aerosol inversions, it is necessary to conduct a sensitivity analysis of the forward model σ. The purpose of this preliminary step is to identify the spectral regions in which the model is most sensitive to the presence of aerosol, and to determine how the signal responds to variations in aerosol particle radius, content and vertical position.

Following this sensitivity study, a set of inversions will be performed, this time extending the state vector to include the retrieval of the aerosol particle radius and content profiles and setting the cloud fraction parameter to 1. In this way we will

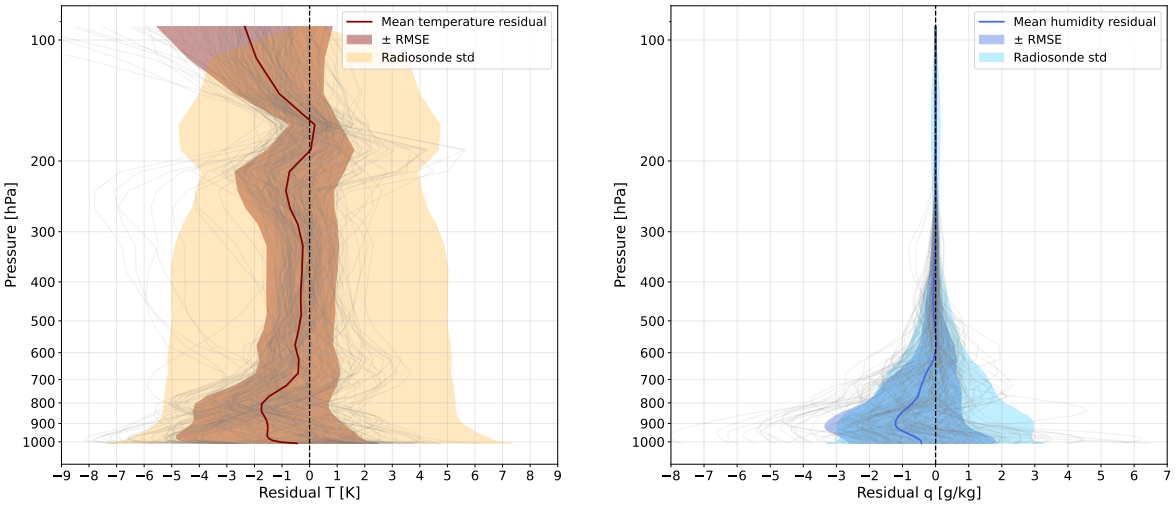

Figure 4.11: *Residuals between retrieved temperature (left) and humidity (right) profiles and the radiosonde considering only cases classified (according to the dust flag) as with aerosol. Grey lines are the single residuals, the red line is the mean residual for temperature, blue line is the mean residual for humidity. The orange (light blue) shaded area is the standard deviation of the temperature (humidity) radiosonde profiles and the shaded red (blue) area is the RMSE between retrieved and radiosonde profiles. All the retrieval are performed considering clear-sky scenes*

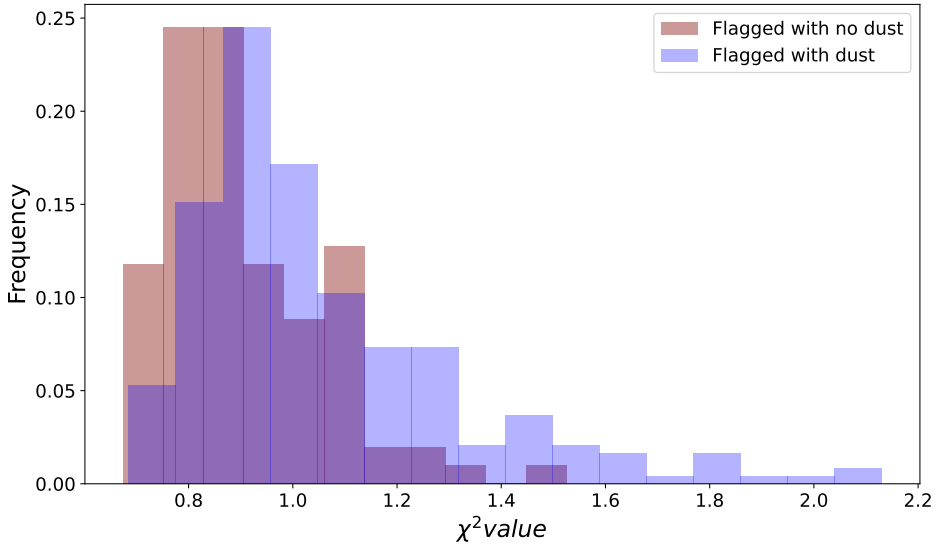

Figure 4.12: *The two χ^2 distribution for cases with no aerosol (red) and with aerosol (blue) according to the classification with the dust flag. All the retrieval are performed considering clear-sky scenes*

be able to evaluate the ability of the algorithm under aerosol conditions and how the inclusion of its retrieval may modify the quality of the fit and the stability of the solution.

4.3.1 Preliminary analysis on synthetic observations

We now focus on analyzing the behavior of the forward model when the presence of aerosol is introduced. In this phase, the cloud fraction parameter cf is set to 1 in order to simulate a fully covered scene, and different values of aerosol effective radius, content and altitude are imposed. In this way we can study the radiative contribution of the aerosol layer modeled in the code, ensuring controlled conditions for the sensitivity analysis.

To select the radius values to be used in the simulations, we relied on the dust aerosol profiles provided by the SAF database [34]. This dataset contains global aerosol vertical profiles, classified into three distinct particle radius ranges: 0.03-0.5 μm, 0.5-5 μm and 5-20 μm. As a first step, the profiles corresponding to the Mediterranean region were extracted. For these profiles basic statistics were performed in order to extract typical values for content and position of the layer of aerosol in the atmosphere.

Using the forward model σ, we simulate radiances for the two seasons, different radii, contents and position of the aerosol layer, and compare them with the radiance simulated in the same conditions but without aerosol, so in a clear-sky condition. The vector state used in these simulations is the same one used as prior/first guess for all the other retrievals, with the exception of the surface temperature (computed from the IASI measurement at 900 cm^{-1} in the retrievals) which is taken from the ERA5 statistics, like the other variables. The simulations are performed in the spectral range [650-1250] cm^{-1}. In this range, we expect an absorption contribution of aerosol, so the radiance simulated at the top of the atmosphere should be smaller than the one simulated in clear-sky.

In Fig.4.13 the prior temperature profile are shown, together with the four pressure levels on which the aerosol layer is considered in the simulations. The prior surface temperature is the vertical red line. We can notice how in the cold months, the prior surface temperature is particularly cold, colder than the atmospheric temperature of the first 3 pressure levels considered for the simulation.

Some of these first aerosol analysis is shown in Fig.4.14 and Fig.4.15 (cold and warm months) where it we can see the the difference between the simulated radiance in case of no aerosol and the one simulated with the presence of a layer of aerosol with a certain effective radius and content.

Two main behaviors emerge: the contribution of the dust has the opposite sign of

the one expected in cold months when the surface temperature used is cooler than the layer where the aerosol is positioned, which is physically consistent but does not reflect the conditions we want to investigate. Considering that we don't actually use these values of first guess surface temperature during our retrievals and that we will focus on warm months (as dust events are more frequent and severe) for the aerosol retrieval, we do not investigate this configuration further. The simulation on the layer 40, whose temperature is cooler than the surface temperature, reflects the typical absorption effect.

For warm months, we can see the positive contribution of aerosol absorption, for all the layers considered. As expected, the absorption effect increases when the content, radius and layer height increase. Aerosol sensitivity is significant across the entire spectral window.

Finally, our last aerosol analysis was performed in order to have an estimate of the sensitivity of the forward model to the optical depth and the radius of the aerosol layer. For each season and level, simulations were carried out with several values of radius and content and for each case the optical depth at 900 cm^{-1} was computed. We then took the value of the difference of the radiance at 900 cm^{-1} between the clear sky simulation and the aerosol one and plotted this difference against the optical depth and the radius. Results are shown in Fig.4.16 for warm months ad in Fig.4.17 for cold months.

For warm months we can see that the radiance difference increases with increasing optical depth and the height of the layer. The sensitivity to particle radius is limited, with exception of high optical depths (which are not likely to be observed), were the black lines start deviating from being vertical.

For cold months, the behavior is quite opposite for the first 3 levels, always to due to the surface temperature effect: the radiance differences are negative (but increase in absolute value with the optical depth). For the higher level, the behavior is similar to the respective warm months.

With this analysis of the spectral radiances, we have been able to investigate the behavior of the forward model in the presence of an aerosol layer. As expected, the impact of aerosol on the radiances is strongest for very large optical depths and for layers located high in the atmosphere. These conditions, however, are not typically representative of real atmospheric scenarios, at least not under standard conditions.

Nevertheless, within the range of interest for this study ($r_{eff} < 2\mu m$ and $OD < 0.2$) the aerosol signal is clearly detectable, In particular, it exceeds the instrumental noise level, indicating that the effect should be observable also in real measurements.

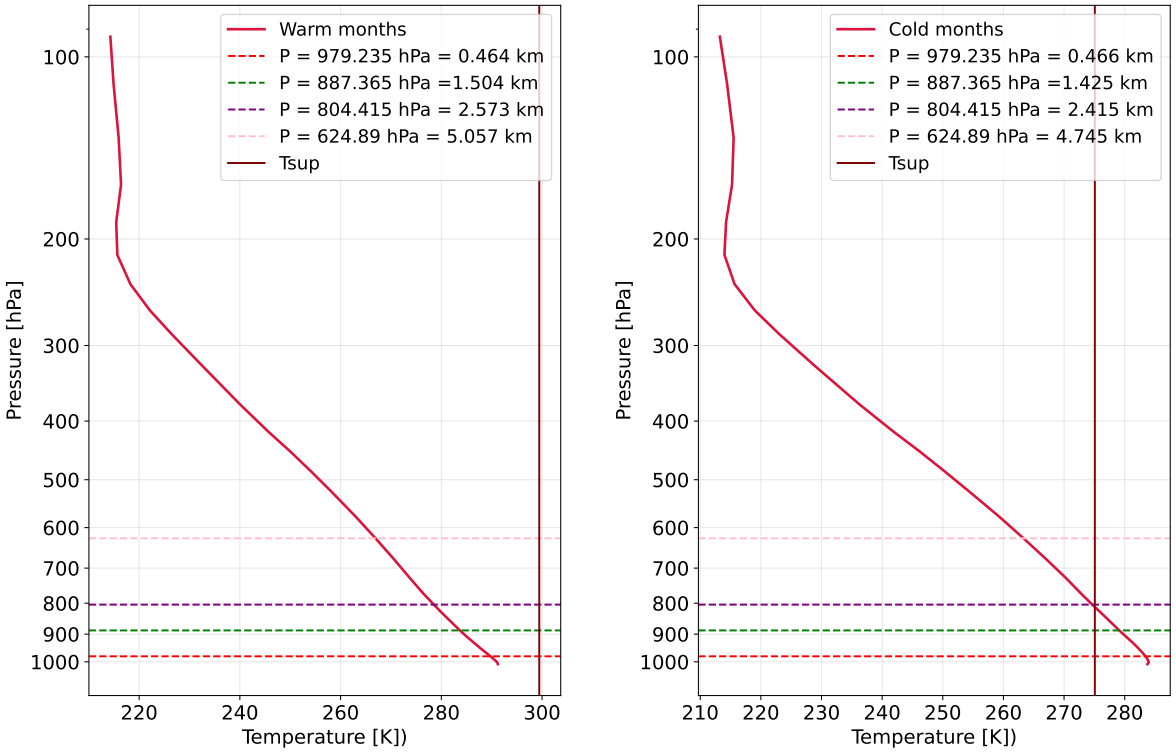

Figure 4.13: *Prior temperature profiles for warm (left panel) and cold (right panel) months up to 100 hPa. The horizontal lines are the pressure levels (with respective height in the legend) for which aerosol sensitivity analysis are performed. The vertical red line is the surface temperature*

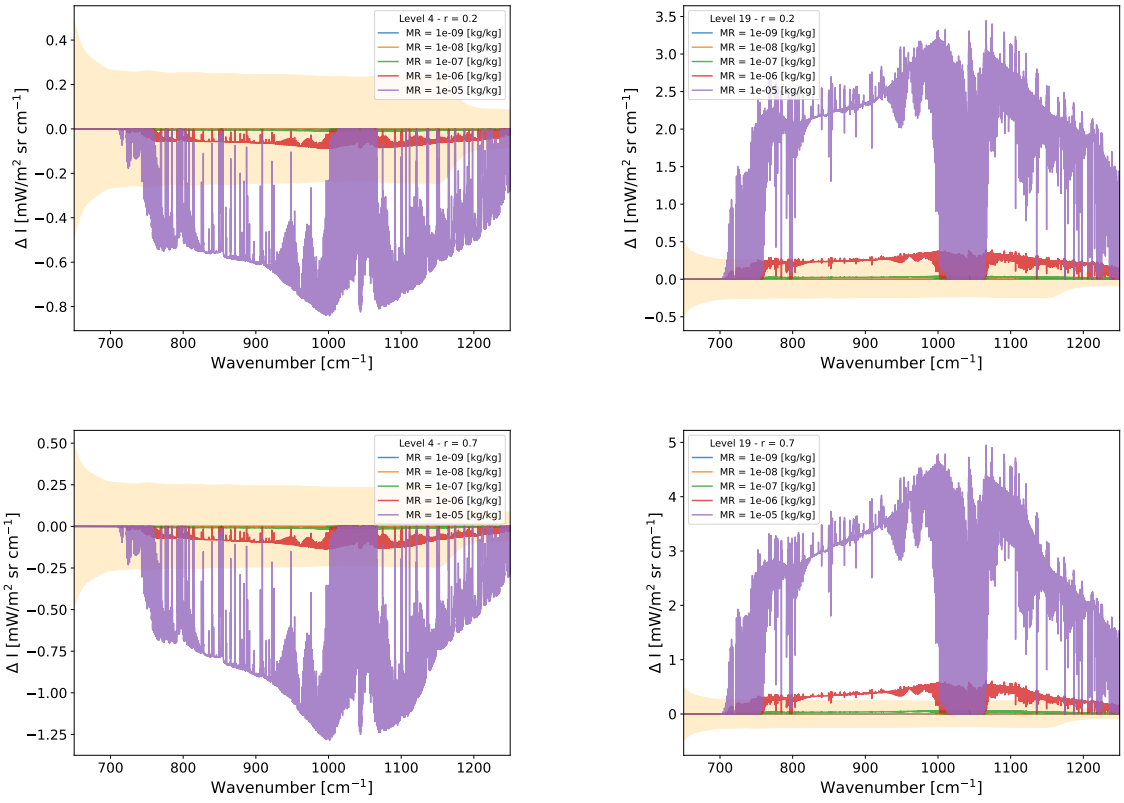

Figure 4.14: *Difference between radiance computed in clear sky condition and the one computed in presence of aerosol. Two radii are shown: 0.2 µm (upper panels) and 0.7 µm (lower panels). Aerosol is positioned in two different pressure layers: level 4 (left panels) and level 19 (right panels). For each panel 5 different values of aerosol content is considered. The yellow shaded area is the IASI measurement error. Cold months are shown*

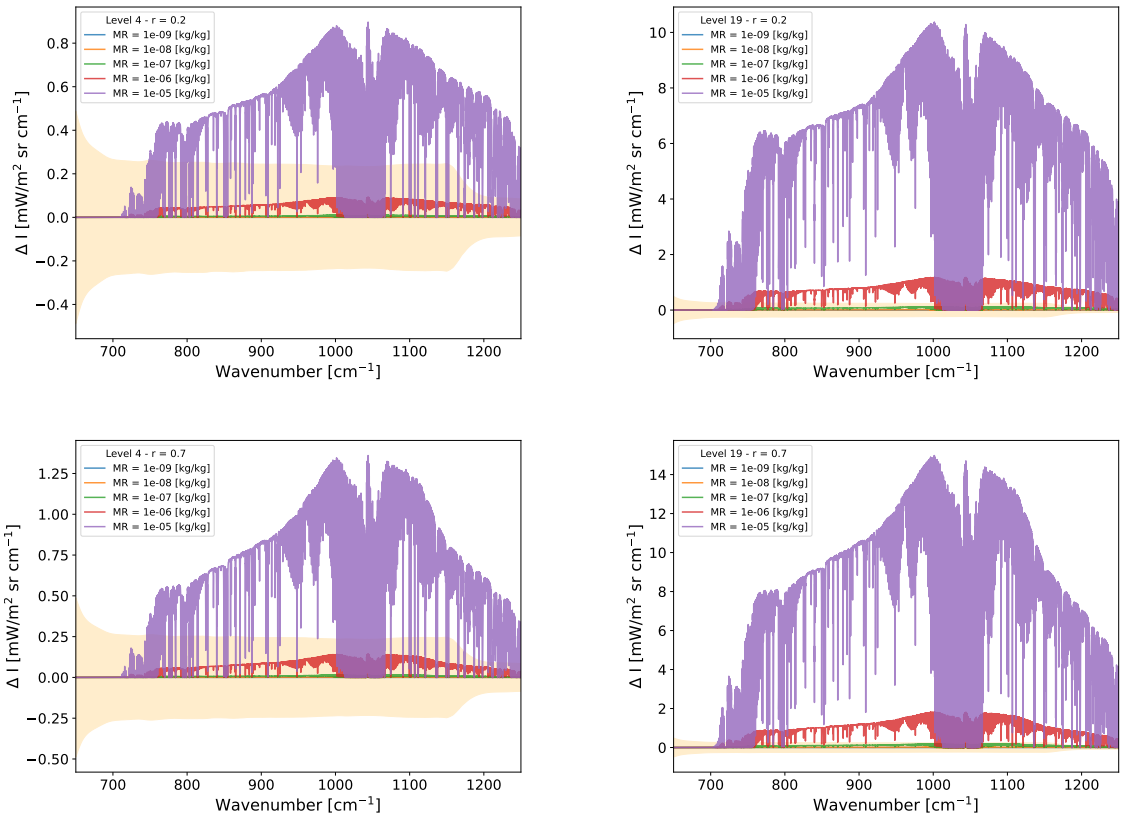

Figure 4.15: *Difference between radiance computed in clear sky condition and the one computed in presence of aerosol. Two radii are shown: 0.2 µm (upper panels) and 0.7 µm (lower panels). Aerosol is positioned in two different pressure layers: level 4 (left panels) and level 19 (right panels). For each panel 5 different values of aerosol content is considered. The yellow shaded area is the IASI measurement error. Warm months are shown*

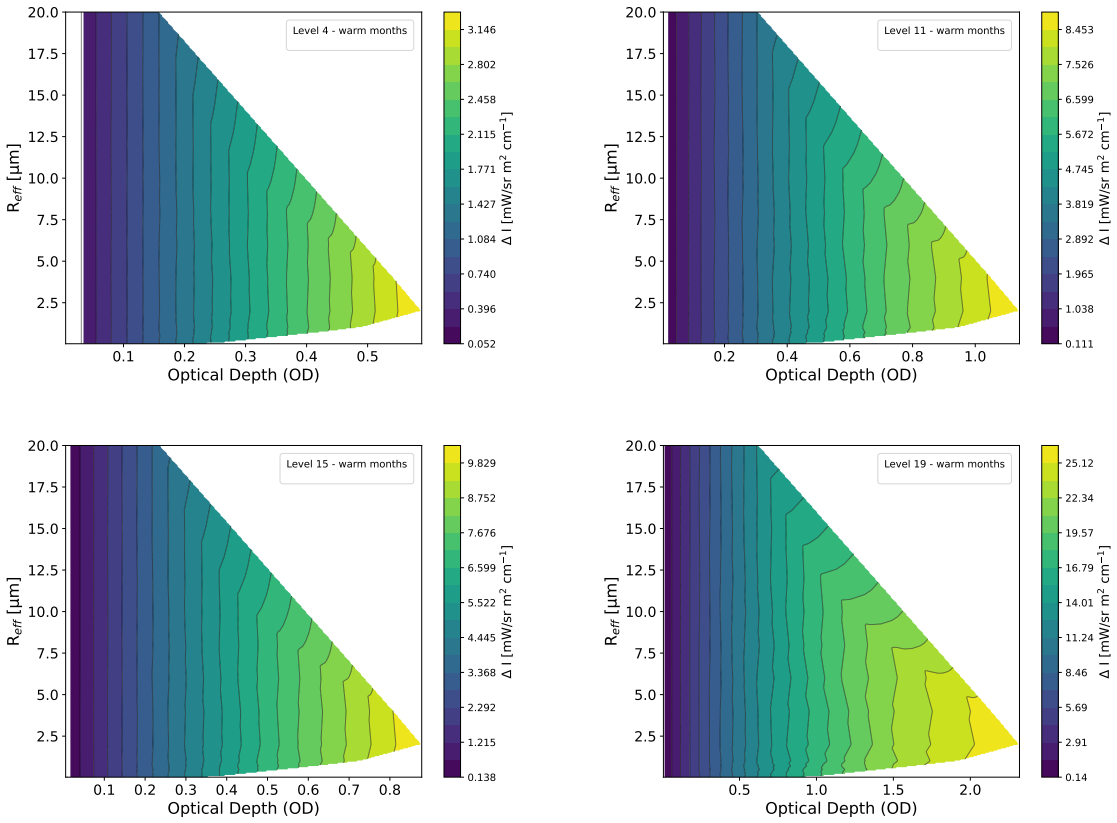

Figure 4.16: *The color represents the difference between the radiance at 900 cm^{-1} between the clear sky simulation and the aerosol simulation. This difference is plotted against the optical depth of the aerosol layer and its effective radius. Note the different scale in the colormap for the 4 different levels. The simulations are performed in the warm months for 4 different pressure layers.*

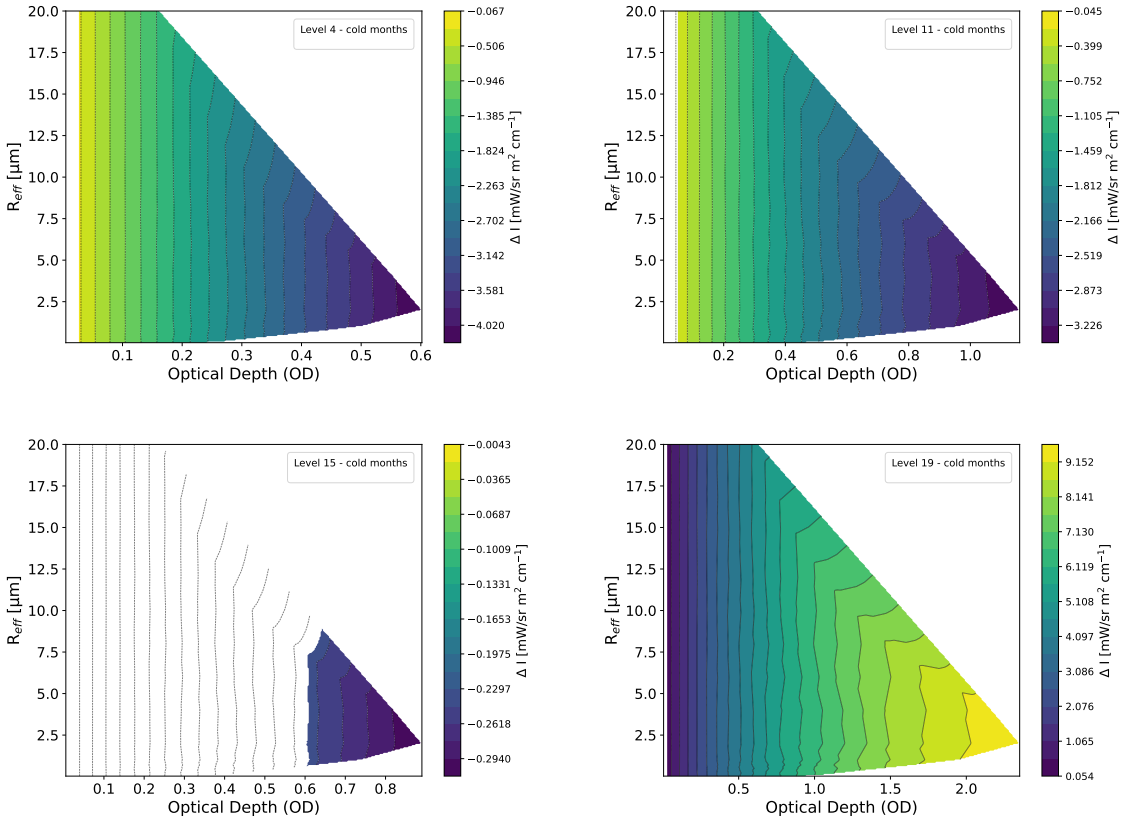

Figure 4.17: *The color represents the difference between the radiance at 900 cm^{-1} between the clear sky simulation and the aerosol simulation. This difference is plotted against the optical depth of the aerosol layer and its effective radius. Note the different scale in the colormap for the 4 different levels. The simulations are performed in the cold months for 4 different pressure layers. The white area covered with black lines is where the difference is smaller than the error in the radiances simulated*

4.3.2 Application to real IASI observations

We now focus exclusively on the actual retrieval on IASI observations. We consider the same cases previously classified as clear-sky and restrict the analysis to the months of July and August. This temporal restriction is due to the fact that we expect a stronger sensitivity in the forward model in these months and, according to the dust flag index and typical seasonal patterns, we expect a higher frequency of transported dust events. We notice that all the days (with exception of two cases) in July and August present a positive dust flag (i.e. bigger than 2), we may therefore expect the presence of aerosol in most of these cases, so it is reasonable to perform the inversion on all of these days.

In the retrieval state vector, we include both the aerosol effective radius and the aerosol content. We used the covariance matrix described in Sec.3.4, in particular the low level matrix was found to perform best best for these retrievals, so we used it for all the cases.

A first feature that emerges from the aerosol retrieval is in the behavior of the iterative process. First of all, the initial guess is farther from the true state than the clear-sky case: the initial values of χ^2 are higher, approximately twice the case without aerosol. This first element highlights the need to better characterize the aerosol first guess. Secondly, the algorithm is in general more unstable. In contrast to the clear-sky cases, where the majority of the inversions converge smoothly without significant divergent or non linear updates, the retrievals including aerosol exhibit a different behavior. When aerosol parameters are introduced into the state vector, the algorithm becomes significantly less stable. This behavior can be attributed to the covariance matrix associated with the aerosol variables, which introduces strong discontinuities and enhanced non-linearities in the inversion process.

The results of these retrievals will be analyzed and compared with those obtained for the same cases under clear-sky conditions. The comparison will be carried out in terms of residuals with respect to radiosonde measurements, as well as in terms of the χ^2 values and spectral residuals. This approach allows us to assess the difference from two perspectives: on one hand, by evaluating the agreement with an independent observing system, and on the other hand, by examining the internal performance of the inversion algorithm through its statistical consistency.

Comparison with radiosonde measurements

Fig.4.18 and Fig.4.19 show the residuals of the temperature and humidity profiles with respect to the radiosonde measurements, for the months of July and August. Specifically, Fig.4.18 refers to the clear-sky retrievals, while Fig.4.19 presents the results

obtained when aerosol is included in the retrieval. All figures show a negative bias, which, as already discussed, most likely originates from the prior information and the first guess used in the inversion.

However, some interesting features can be identified. In particular, the bias is smaller in the retrievals including aerosol, for both temperature and humidity. Regarding the RMSE, a reduction is observed in the aerosol case for temperature, whereas it remains nearly unchanged for humidity.

The most interesting feature concerns the behavior of the largest temperature residuals. In the clear-sky retrievals, particularly large deviations are observed up to around 200 hPa for a subset of cases. These pronounced residuals disappear when aerosol is included in the retrieval.

This negative temperature bias observed in the retrievals performed without aerosol is likely the result of a compensation effect. Since aerosol exerts an absorptive effect, the radiance measured by the satellite is lower than it would be under truly aerosol-free conditions. However, if the model does not account for the presence of aerosol this reduction in the measured signal cannot be attributed to aerosol absorption. Instead, the inversion algorithm compensates by adjusting the other state variables. In particular, a decrease in temperature leads to a reduction in the simulated radiance, thereby improving the agreement with the observed signal. While this adjustment reduces the radiance residuals, it drives the retrieved temperature profile away from the 'true' (radiosonde) atmospheric state, resulting in a negative bias.

These cases disappear in the retrievals that include aerosol most likely because the algorithm is then able to correctly attribute part of the observed absorption to the presence of aerosol. As a consequence, it no longer needs to compensate for the missing absorption by modifying the temperature profile.

One important aspect to highlight is that the presence of the negative bias with respect to radiosonde observations in the clear-sky retrievals (Fig.4.1) has been attributed both to the presence of a similar bias in the first guess (Fig.3.9) and to a compensating effect on the retrieved temperature caused by the lack of aerosol representation in the retrieval. It is likely that both factors contribute to the observed bias, and it is not straightforward to clearly disentangle their respective roles. However, the fact that the bias decreases when aerosol is included in the retrieval represents a significant improvement. This is particularly evident in the cases that show a strong bias between 600 and 200 hPa (Fig.4.18) in the aerosol-free retrievals which disappears when aerosol is taken into account (Fig.4.19).

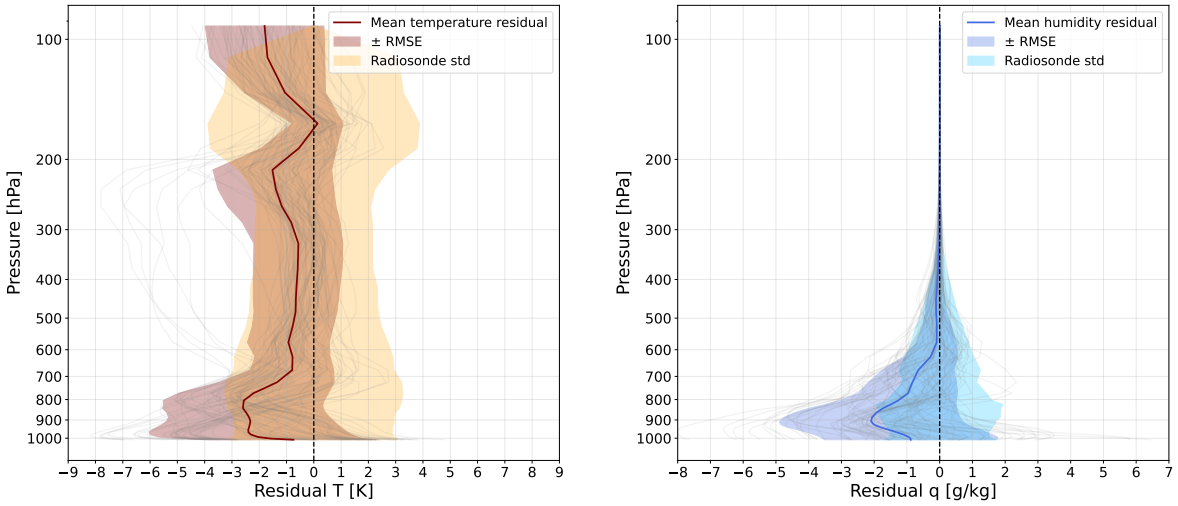

Figure 4.18: *Residuals between retrieved temperature (left) and humidity (right) profiles and the radiosonde measurements. Retrievals are performed in clear-sky conditions for July and August. Grey lines are the single residuals, the red line is the mean residual for temperature, blue line is the mean residual for humidity. The orange (light blue) shaded area is the standard deviation of the temperature (humidity) radiosonde profiles and the shaded red (blue) area is the RMSE between retrieved and radiosonde profiles.*

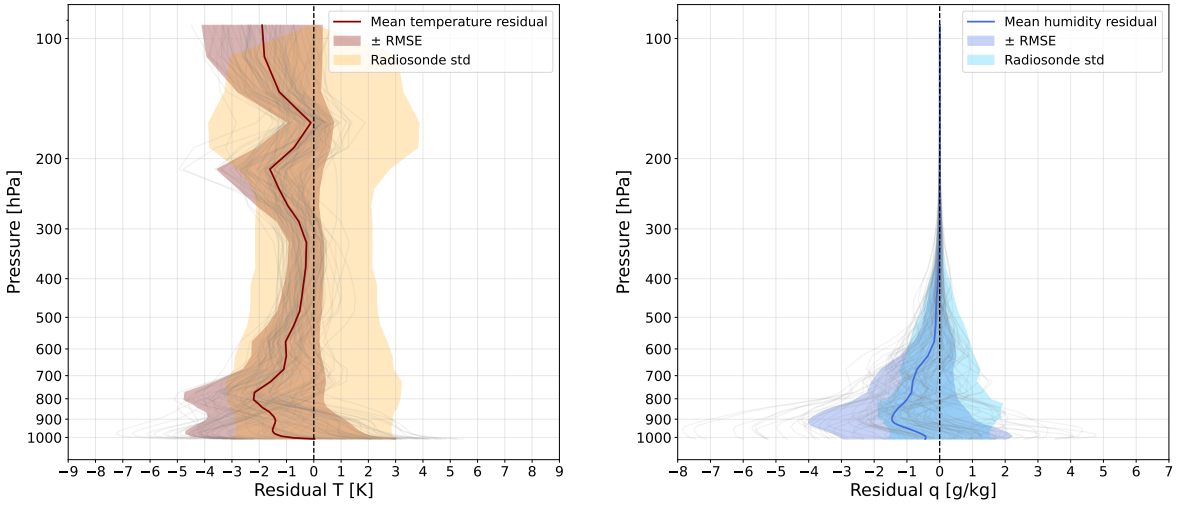

Figure 4.19: *Residuals between retrieved temperature (left) and humidity (right) profiles and the radiosonde measurements. Retrievals are performed in aerosol conditions for July and August. Grey lines are the single residuals, the red line is the mean residual for temperature, blue line is the mean residual for humidity. The orange (light blue) shaded area is the standard deviation of the temperature (humidity) radiosonde profiles and the shaded red (blue) area is the RMSE between retrieved and radiosonde profiles.*

Statistical analysis: χ^2

We now investigate how the performance of the algorithm changes when aerosol retrieval is included, starting from the analysis of the χ^2 values. Fig.4.20 shows a scatter plot of the χ^2 versus the dust flag index. In order to improve the readability of the figure and highlight the underlying trend, the χ^2 values have been averaged over dust flag intervals of width 5. The most evident result is that, for all dust flag bins, the mean χ^2 values decrease when aerosol is included in the retrieval. The standard deviations (the red and green bars) and their upper limits are smaller for the dust retrieval.

This systematic reduction indicates an overall improvement in the quality of the fit between simulated and observed radiance under dusty conditions: this is a first sign that accounting for aerosol in the state vector, when dust presence is suspected, leads to a more consistent representation of the measured signal. Another interesting result is that some cases that failed to converge in the clear-sky retrieval do converge when aerosol is included in the inversion.

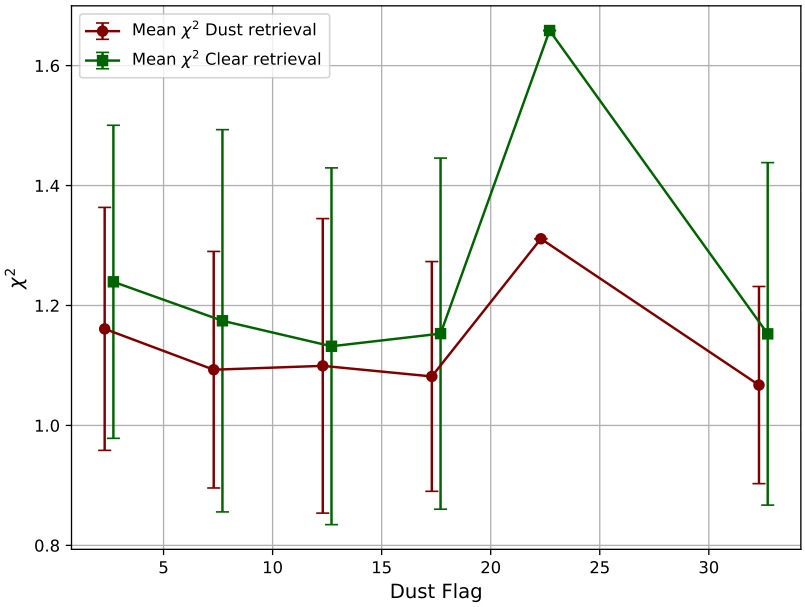

Figure 4.20: *Scatter plot between χ^2 values and dust flag. The green line refers to clear sky retrievals while the red one to aerosol retrievals. The χ^2 values are averaged over bins of width 5. Vertical bars are the standard deviation*

Case studio: 12 July

We now focus on a particularly interesting case study, namely the retrieval performed on 12 July 2023. This case exhibits markedly different behavior depending on the assumptions adopted in the forward model. Under clear-sky conditions, the retrieval does not reach convergence. In contrast, when aerosol is included in the state vector,

the inversion successfully converges. According to the dust flag index, this measurement is associated with a strong presence of aerosol (dust index = 35). Independent observations from Copernicus Atmosphere Monitoring Service (CAMS) analyses and MODIS satellite measurements also confirm the presence of transported dust over the region during those days.

Fig.4.21 shows retrieved profiles of temperature and humidity for the clear sky retrieval and the aerosol one compared with the radiosonde measurement. Fig.4.22 shows the spectral residual for the two retrievals. The improvement is evident across all figures. On one hand, both the temperature and humidity profiles move closer to the radiosonde measurements. On the other hand, the spectral residuals, which in the clear-sky retrieval exhibit features of an inversion that was not successful, appear significantly cleaner when aerosol is included, particularly in the window region.

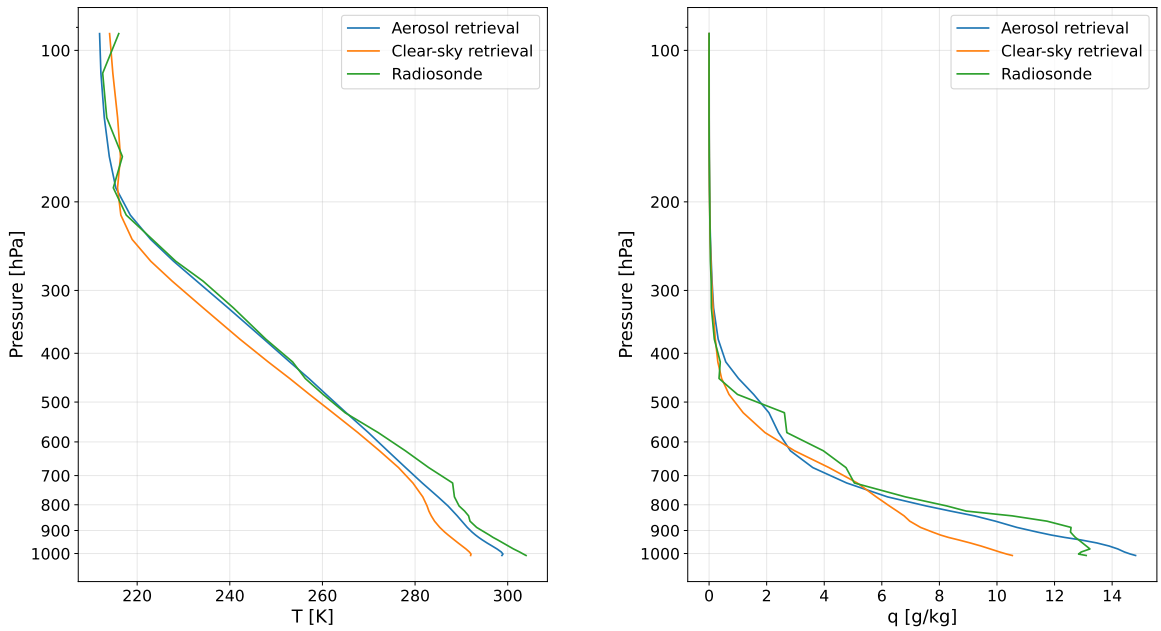

Figure 4.21: *Temperature (left panel) and humidity (right panel) profiles up to 100 hPa for 12/07. The orange line is the retrieved profile in clear sky conditions, the blue one in aerosol condition. The green line is the radiosonde measurement*

General considerations

The analysis presented here represents a preliminary investigation of the capability of the inversion framework to retrieve aerosol signatures from IASI radiances. Although the results obtained are encouraging and suggest that the inclusion of aerosol param-

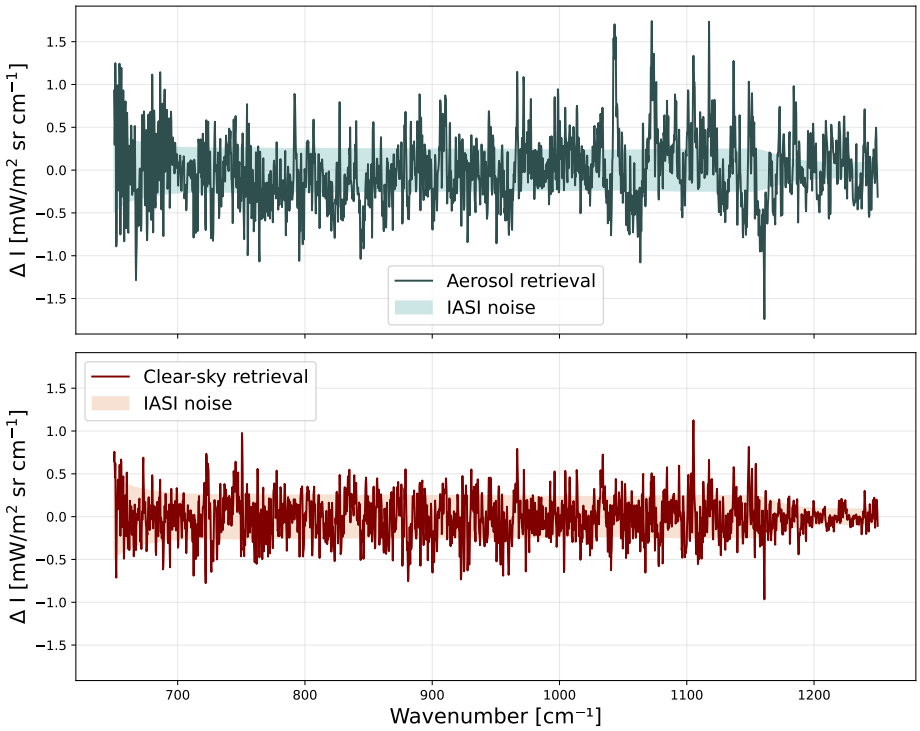

Figure 4.22: *Spectral residual for 12/07. In the green upper panel residuals of the clear-sky retrieval while in the red lower panel the residual of the aerosol retrieval*

eters can improve the spectral fit in certain cases, these findings should be interpreted with caution and considered as an initial step toward a more comprehensive assessment of aerosol retrieval capabilities.

First, the retrieval configuration adopted in this study has not yet been fully optimized. In particular, further tuning of several algorithm parameters would likely be necessary to ensure a more robust characterization of aerosol effects in the inversion procedure. The current setup should therefore be regarded as a baseline configuration rather than a fully optimized retrieval system. Moreover, the identification of dust-contaminated scenes in this analysis relied on the IASI dust flag product. While this classification provides a useful first indication of the presence of mineral dust, it remains an indirect proxy and may introduce uncertainties in the selection of aerosol cases. For this reason, the interpretation of the results would benefit from additional independent information on aerosol presence and intensity.

In addition, the role of surface emissivity deserves careful attention. In hyperspectral infrared retrievals, the surface emissivity often acts as an additional degree of freedom that can partially compensate for spectral residuals associated with imperfect forward modeling. A systematic analysis of the emissivity values retrieved by the inversion algorithm would therefore be necessary to determine whether part of the observed improvement in the spectral fit is actually related to changes in surface

emissivity rather than to the presence of aerosol in the atmosphere.

Finally, a rigorous quantitative evaluation of aerosol retrieval performance would require comparison with independent observations of dust loading. Such validation remains challenging, as suitable collocated measurements are often limited in space and time. Nevertheless, comparisons with independent datasets would be essential in order to assess the quantitative reliability of the retrieved aerosol parameters. This step is particularly important considering that any satellite-derived product ultimately requires validation against independent measurements to establish its scientific credibility.

In this context, the results obtained in this study should therefore be interpreted as a first exploratory analysis that highlights the potential of the inversion framework to account for aerosol effects in hyperspectral infrared radiances. Further work will be required to refine the retrieval configuration, improve the characterization of aerosol scenes, and perform a more rigorous quantitative validation of the retrieved aerosol properties.

Chapter 5

Conclusions

This thesis addressed a central problem in hyperspectral infrared remote sensing: the physically consistent inversion of satellite radiances under atmospheric conditions that go beyond the ideal clear-sky assumption.

While operational clear-sky products are well established, extending retrieval methodologies to more realistic all-sky conditions remains an important scientific challenge. Clear-sky conditions occur only over a limited fraction of the atmosphere, so it is crucial to develop approaches capable of providing accurate products also in the presence of clouds and aerosols. However, this is typically not pursued operationally because the presence of scattering particles significantly complicates the retrieval scheme.

Within this framework, the objective of this work was to assess the performance of the IOTA inversion algorithm coupled with the σ forward model when applied to IASI observations, first under clear-sky conditions and then in scenes affected by mineral dust aerosols.

The σ model is a fast radiative transfer model designed to efficiently simulate infrared radiances in both clear and scattering atmospheres. Thanks to the Chou approximation, the treatment of scattering is significantly simplified, allowing the use of the same formalism adopted in clear-sky conditions, even in the presence of scattering particles. The model also provides analytical Jacobians for both the atmospheric state variables and the microphysical properties and concentrations of clouds or aerosols.

The IOTA algorithm is an inversion scheme based on the Optimal Estimation method. Through the use of principal component compression, the dimensionality of the problem is reduced, significantly decreasing the computational cost while preserving the essential information content of the observations. Furthermore, the construction of smoothed ad-hoc prior covariance matrices for aerosols enables the retrieval of physically consistent vertical profiles of dust content and effective particle size while stabilizing the inversion.

The initial steps of this work involved the construction of the prior distributions and the tuning of the retrieval algorithm parameters. The first part of the analysis focused on temperature and water vapor retrievals in clear-sky conditions; the retrieved profiles were evaluated through comparisons with collocated radiosonde measurements. The comparison with radiosondes highlights the presence of a negative bias, particularly marked near the surface indicating that the retrieval tends to underestimate the atmospheric variable compared to the in situ observations. This negative bias is consistent with the bias already present in the prior and first-guess profiles with respect to the radiosondes. This behavior suggests that part of the discrepancy originates from the initial atmospheric state used in the inversion and that the retrieval, although improving the fit to the radiances, still retains some dependence on the background information. These biases highlight the need for a more representative prior and first-guess state.

Despite these limitations, one of the clearest outcomes of the clear-sky inversion is the strong improvement achieved by the retrievals in terms of spectral consistency. The algorithm produces a substantial reduction of the χ^2 values and of spectral residuals when comparing the initial distribution based on the first guess to the final one, based on the retrieved state. This systematic reduction represents a key indicator that the retrieval is effectively adjusting the atmospheric state in a physically meaningful direction to better explain the observations. In this sense, the clear-sky results provide a solid baseline demonstrating that the algorithm is numerically stable and capable of significantly improving the fit to the measured radiances.

The second part of the thesis explored the extension toward aerosol-affected conditions, with a focus on dust. The preliminary analysis indicates that the σ forward model shows sensitivity to aerosol signatures in the thermal infrared, suggesting that the inversion framework can exploit this sensitivity under favorable conditions. The aerosol analysis was conducted using observations acquired during the summer months. In the cases analyzed, the inclusion of aerosol parameters in the state vector leads to encouraging results. In several situations, accounting for aerosol improves the spectral fit, with reductions in χ^2 values and in residual structures in the window regions where dust signatures are expected. In addition, some improvements are observed in the comparisons with radiosonde profiles. In particular, the negative bias observed in the retrievals with respect to the radiosondes is reduced when aerosol is included in the inversion. This behavior is physically consistent with the radiative effect of mineral dust in the thermal infrared. These results demonstrate that the IOTA inversion algorithm can robustly handle the presence of aerosols. Retrieving aerosol properties not only enables their characterization, but also improves the realism of temperature and humidity retrievals in atmospheres affected by aerosol scattering.

Despite these encouraging results, several limitations remain and indicate directions for future work. A first aspect concerns the characterization of the initial atmospheric state. The initial temperature, humidity, and aerosol profiles were not found to be fully adequate, and this affects the quality of the retrieval. Improving the first-guess information therefore represents an important step for both the clear-sky and aerosol retrievals.

In addition, the aerosol retrieval component would benefit from a more systematic assessment of the model configuration: further work should include a dedicated tuning of the model parameters to improve inversion stability. Furthermore, a more detailed analysis of the role of surface emissivity and surface temperature in the simulations should be investigated. These factors can significantly influence the radiative signal in the thermal infrared and therefore affect the stability of the inversion. Another limitation of this work is that the aerosol analysis presented was limited to summer conditions. Extending the study to a full annual cycle will be necessary to properly evaluate the performance of the algorithm under a wider range of atmospheric regimes and aerosol loading conditions. Finally, the analysis focused exclusively on transported dust aerosols. Future work should therefore extend the investigation to different aerosol types and models, allowing for a more comprehensive optimization of the aerosol optical properties and particle size distributions.

Overall, the results obtained in this work are encouraging and indicate that the proposed retrieval framework provides a promising basis for future developments and for further studies aimed at improving all-sky infrared retrievals.

Bibliography

[1] ESA. About IASI. https://www.esa.int/Applications/Observing_the_Earth/Meteorological_missions/MetOp/About_IASI, 2020.

[2] M. Maahn, D. D. Turner, U. Löhnert, D. J. Posselt, K. Ebell, G. G. Mace, and J. M. Comstock. Optimal estimation retrievals and their uncertainties - what every atmospheric scientist should know. *BAMS Article - AMERICAN METEOROLOGICAL SOCIETY*, 2020.

[3] C. D. Rodgers. Retrieval of atmospheric temperature and composition from remote measurements of thermal radiation. *REVIEWS OF GEOPHYSICS AND SPACE PHYSICS*, 1976.

[4] F. Hilton, K. Bowman, R. Saunders, J. Xu, A. Lee, X. Calbet, C. Clerbaux, A. Griesfeller, M. Loiselet, A. P. McNally, F. Pelek, W. L. Smith, and S. Walsh. Hyperspectral earth observation from IASI: Five years of accomplishments. *Bulletin of the American Meteorological Society*, 93(3):347–370, 2012. Review article on IASI performance and applications.

[5] T. August, A. K. Heidinger, M. Goldberg, J. Hocking, D. O'Brien, A. P. McNally, X. Xiong, Y. Chen, J. Li, W. L. Smith, and P. Bailey. IASI on MetOp-A: Operational level 2 retrievals after five years in orbit. *Journal of Quantitative Spectroscopy and Radiative Transfer*, 113(11):1340–1371, 2012.

[6] EUMETSAT. Validation Report IASI Level2 T and Q profiles release 1.1 extension, 2022.

[7] EUMETSAT. IASI Level 2 - Temperature and Humidity Profiles. https://navigator.eumetsat.int/product/EO:EUM:DAT:METOP:EARS-IASI-L2, 2017.

[8] N. Pougatchev, T. August, X. Calbet, T. Hultberg, O. Oduleye, P. Schlüssel, B. Stiller, K. St. Germain, and G. Bingham. Validation of the iasi temperature and water vapor profile retrievals by correlative radiosondes. 2008.

[9] N. Pougatchev, T. August, X. Calbet, T. Hultberg, and P. Oduleye, O.and Schlüssel. Iasi temperature and water vapor retrievals – error assessment and validation. *European Geosciences Union*, 2009.

[10] IPCC. Climate change 2021: The physical science basis. contribution of working group i to the sixth assessment report of the intergovernmental panel on climate change, 2021.

[11] L. A. Remer, Y. J. Kaufman, D. Tanre, S. Mattoo, D. A. Chu, J. V. Martins, R.-R. Li, C. Ichoku, R. C. Levy, R. G. Kleidman, T. F. Eck, E. Vermote, and B. N. Holben. The modis aerosol algorithm, products, and validation. *IEEE TRANSACTIONS ON GEOSCIENCE AND REMOTE SENSING*, 2002.

[12] J.V. Martonchik, D. J. Diner, K. A. Crean, and M. A. Bull. Regional aerosol retrieval results from misr. *American Meteorological Society*, 2004.

[13] V. Capelle, A. Chédin, M. Pondrom, C. Crevoisier, R. Armante, L. Crépeau, and N. A. Scott. Infrared dust aerosol optical depth retrieved daily from iasi and comparison with aeronet over the period 2007–2016. *Remote Sensing of Environment*, 206:15–31, 2018.

[14] T. Maestri, M. Martinazzo, W. Cossich, C. Serio, G. Masiello, and S. Venafra. Fast radiative transfer in multiple scattering atmospheres at far and mid infrared wavelengths. *AIP Conference Proceedings*, 2024.

[15] C. Serio, G. Masiello, G. Liuzzi, A. Cersosimo, T. Maestri, M. Martinazzo, F. Masin, G. Proietti Pelliccia, S. Venafra, and C. Camy-Peyret. Demonstration of a physical inversion scheme for all-sky, day-night iasi observations and application to the analysis of the onset of the antarctica ozone hole: Assessment of retrievals and consistency of forward modeling. *Journal of Quantitative Spectroscopy and Radiative Transfer*, 2024.

[16] M. Martinazzo, D. Magurno, W. Cossich, C. Serio, G. Masiello, and T. Maestri. Assessment of the accuracy of scaling methods for radiance simulations at far and mid infrared wavelengths. *Journal of Quantitative Spectroscopy and Radiative Transfer*, 2021.

[17] Ming-Dah Chou, Kyu-Tae Lee, Si-Chee Tsay, and Qiang Fu. Parameterization for cloud longwave scattering for use in atmospheric models. *Journal of Climate, Volume 12, Issue 1*, 1999.

[18] EUMETSAT. IASI Level 1: Product Guide. https://user.eumetsat.int/s3/eup-strapi-media/pdf_iasi_pg_487c765315.pdf, 2019.

[19] S. Callewaert, S. Vandenbussche, N. Kumps, A. Kylling, X. Shang, M. Komppula, P. Goloub, and M. De Maziere. The mineral aerosol profiling from infrared radiances (mapir) algorithm: version 4.1 description and evaluation. *Atmospheric measrument techniques*, 2019.

[20] S. Vandenbussche, S. Kochenova, A. C. Vandaele, N. Kumps, and M. De Mazière. Retrieval of desert dust aerosol vertical profiles from iasi measurements in the tir atmospheric window. *Atmospheric measrument techniques*, 2013.

[21] D.S. Sergio, L. Larrabee Strow, A. Tangborn, X. Huang, X. Chen, X. Liu, W. Wu, and Q. Yang. Single-footprint retrievals for airs using a fast twoslab cloud-representation model and the sarta all-sky infrared radiative transfer algorithm. *Atmospheric measurements techniques*, 2018.

[22] G. Masiello, C. Serio, T. Maestri, M. Martinazzo, F. Masin, G. Liuzzi, and S. Venafra. The new σ-iasi code for all sky radiative transfer calculations in the spectral range 10 to 2760 cm-1: σ-iasi/f2n. *Journal of Quantitative Spectroscopy and Radiative Transfer*, 2024.

[23] G. Liuzzi, G. Masiello, C. Serio, S. Venafra, and C. Camy-Peyret. Physical inversion of the full iasi spectra: Assessment of atmospheric parameters retrievals, consistency of spectroscopy and forward modelling. *Journal of Quantitative Spectroscopy & Radiative Transfer*, 2016.

[24] ARPAE. Radiosondaggio atmosferico automatico. https://www.arpae.it/it/temi-ambientali/meteo/dati-e-osservazioni/radiosondaggio, 2020.

[25] U Amato, G Masiello, C Serio, and M Viggiano. The sigma-iasi code for the calculation of infrared atmospheric radiance and its derivatives. *Environmental Modelling and Software*, 2002.

[26] K. N. Liou. *An Introduction to Atmospheric Radiation*. Academic Press, 525 B Street, Suite 1900, San Diego, California 92101-4495, USA, 2002.

[27] O. Pena and U Pal. Scattering of electromagnetic radiation by a multilayered sphere. *Computer Physics Communications*, 2009.

[28] H. Downing, D. and D Williams. Optical constants of water in the infrared. *Journal of Geophysical Research*, 1975.

[29] L. Yang, P.and Bi, B. A. Baum, K. Liou, G. W. Kattawar, M. I. Mishchenko, and B. Cole. Spectrally consistent scattering, absorption, and polarization properties of atmospheric ice crystals at wavelengths from 0.2 to 100 μm. *JOURNAL OF THE ATMOSPHERIC SCIENCES*, 2012.

[30] jrmascio. Line-By-Line Radiative Transfer Model by Atmospheric and Environmental Research. https://github.com/AER-RC/LBLRTM.

[31] Clive D. Rodgers. *INVERSE METHODS FOR ATMOSPHERIC SOUNDING-Theory and Practice*. World Scientific Publishing Co. Pte. Ltd., P O Box 128, Farrer Road, Singapore 912805, 2000.

[32] D. D. Turner and U Lohnert. Information content and uncertainties in thermodynamic profiles and liquid cloud properties retrieved from the ground-based atmospheric emitted radiance interferometer (aeri). *JOURNAL OF APPLIED METEOROLOGY AND CLIMATOLOGY*, 2013.

[33] H. W. Press, A. S. Teukolsky, T. W. Vetterling, and P. B. Flannery. *Numerical Recipes in FORTRAN- The Art of Scientific Computing*. Press Syndicate of the University of Cambridge, The Pitt Building, Trumpington Street, Cambridge CB2 1RP, 1995.

[34] A. P. McNally R. Eresmaa. Diverse profile datasets from the ECMWF 137-level short-range forecasts. https://www.researchgate.net/publication/268486012_Diverse_profile_datasets_from_the_ECMWF_137-level_short-range_forecasts/citations.

[35] Shlens Jonathon. A tutorial on principal component analysis, https://arxiv.org/abs/1404.1100. 2014.

[36] Stella E. I. Manavi, Andreas Aktypis, Evangelia Siouti, Ksakousti Skyllakou, Stelios Myriokefalitakis, Maria Kanakidou, and Spyros N. Pandis. Atmospheric aerosol spatial variability: Impacts on air quality and climate change. *One Earth*, 2025.

[37] NASA. Aerosols and Their Importance. https://earth.gsfc.nasa.gov/climate/data/deep-blue/aerosols.

[38] C. Di Biagio, E. Bru, A. Orta, S. Chevaillier, C. Baldo, A. Bergé, M. Cazaunau, S. Lafon, S. Nowak, E. Pangui, M. O. Andreae, P. Dagsson-Waldhauserova, K. Dintwe, K. Kandler, J. S. King, A. Chaput, G. S. Okin, S. Piketh, T. Saeed, D. Seibert, Z. Shi, E. Williams, P. Sellitto, and P. Formenti. Mid- and far-infrared

spectral signatures of mineral dust from low- to high-latitude regions: significance and implications. *Atmospheric Chemistry and Physics*, 2026.

[39] University of Wyoming. University of Wyoming Atmospheric Science Radiosonde Archive. https://weather.uwyo.edu/upperair/sounding.shtml.

[40] C. Biskas, K. Michailidis, E. Koukouli M., and D. Balis. Evaluation of the iasi/metop dust flag product using aeronet data. *atmosphere*, 2025.

[41] Climate Data Store. Complete ERA5 global atmospheric reanalysis. https://cds.climate.copernicus.eu/datasets/reanalysis-era5-complete?tab=overview, 2025.

[42] ECMWF. Pressure on model levels. https://confluence.ecmwf.int/plugins/viewsource/viewpagesrc.action?pageId=158636068.

[43] ECMWF. L137 model levels definitions. https://confluence.ecmwf.int/display/UDOC/L137+model+level+definitions.

[44] ECMWF. IFS DOCUMENTATION-PART IV: PHYSICAL PROCESSES. https://www.ecmwf.int/sites/default/files/elibrary/2021/81271-ifs-documentation-cy47r3-part-iv-physical-processes_1.pdf, 2021.

[45] huang research group. A global data set of surface spectral emissivity for GCM and NWP use. https://huang.engin.umich.edu/182-2/.

[46] ICOS. STANDARDISED GREENHOUSE GAS MEASUREMENTS THROUGHOUT EUROPE. https://www.icos-cp.eu.

[47] Z. Sun. 'parametrization of effective sizes of cirrus-cloud particles and its verification against observations'. *Quarterly Journal of the Royal Meteorological Society*, 2001.